Ore Geology Reviews 119 (2020) 103325

Contents lists available at ScienceDirect

Ore Geology Reviews

journal homepage: www.elsevier.com/locate/oregeorev

Host minerals of Li–Ga–V–rare earth elements in Carboniferous karstic bauxites in southwest China

Kun-Yue Ling[a], Hao-Shu Tang[a], Zheng-Wei Zhang[a,*], Han-Jie Wen[a,b,*]

[a] State Key Laboratory of Ore Deposit Geochemistry, Institute of Geochemistry, Chinese Academy of Sciences, Guiyang 550081, China
[b] University of Chinese Academy of Sciences, Beijing 100049, China

ARTICLE INFO

Keywords:
Karstic bauxite
Trace element
Host mineral
LA–ICP–MS

ABSTRACT

The Carboniferous karstic bauxite-bearing rock series in central Guizhou Province in southwest (SW) China is rich in trace elements, particularly Li, Ga, V, and rare earth elements (REEs), which have potential for comprehensive utilization as independent deposits or associated resources. However, the host minerals of Li, Ga, V, and REEs are not well-constrained because the sedimentary rocks are characteristics by complex mineral composition and fine mineral particles. This situation considerably hinders the compressive utilization of these trace elements in bauxite. Herein, laser ablation–inductively coupled plasma–mass spectrometry (LA–ICP–MS) was successfully applied to element geochemistry analysis of hydrous minerals (diaspore/boehmite, kaolinite, and illite) in karstic bauxite samples, based on the principle that laser ablation data of all oxides were normalized to the sum of 100% minus the total volatile components of the mineral chemical formula. The analysis showed signal stabilization. Results indicated that the bivariate plots of selected elements had characteristics similar to statistical results of whole-rock samples from global bauxites, thereby indicating that the LA–ICP–MS analysis data were reliably but artificially herein. Combined with whole-rock geochemistry studies, the analysis results revealed that smectite may be the main host minerals of Li. Furthermore, Ga was enriched in diaspore/boehmite; V was mainly enriched in iron-bearing minerals, particularly chlorite; and REE-independent minerals, such as monazite, were the main host minerals of REEs in the Carboniferous karstic bauxite in SW China. This study contributed to the knowledge on the use of in-situ method for the element geochemistry investigation of hydrous minerals and sedimentary rocks.

1. Introduction

Recent studies revealed that karstic bauxite-bearing rock series around the world are rich in trace elements, including Li, Ga, V, Ti, Zr, Hf, Nb, Ta, and rare earth elements (REEs) (e.g., Mameli et al., 2007; Li et al., 2013; Liu et al., 2016; Ahmadnejad et al., 2017; Mongelli et al., 2017; Ling et al., 2018). It has the potential for comprehensive utilization as independent deposits or associated resource (Wang et al., 2010, 2013). Understanding host mineral and mode of occurrence of these trace elements in bauxites are important in assessing the economic potential of bauxite deposits. The elements Ti, Nb, and Ta are mainly enriched in Ti-dioxide mineral, and the elements Zr and Hf are controlled by zircon in bauxites (Mordberg et al., 2001; Liu et al., 2013; Gao and Liu, 2014). These elements are considered immobile during ore-forming processes and ultimately become enriched in bauxite-bearing rocks (Calagari and Abedini, 2007; Liu et al., 2013; Mongelli et al., 2014, 2016; Zamanian et al., 2016). However, the host minerals of Li, Ga, V, and REEs are not well-constrained because bauxite samples show fine mineral particles and complex mineral composition. Thereby, the comprehensive utilization of these trace elements is largely hindered in bauxite, even though Ga and V have been successfully extracted as by-products of Al production (Calagari and Abedini, 2007; Wang et al., 2012; Hanilçi, 2013).

Laser ablation–inductively coupled plasma–mass spectrometry (LA–ICP–MS) is an excellent instrument for in-situ elemental geochemical analysis and it provides an effective method to reveal the chemical composition of minerals. However, except for a few rock types, such as conglomerate and sandstone, the majority of sedimentary rocks have been barely studied by in-situ analysis methods in the last century, because the mineral particles of sedimentary rock, including bauxite, are smaller than 10 μm, which is much smaller than the diameter of the laser beam (typically greater than 32 μm) used in

* Corresponding authors at: State Key Laboratory of Ore Deposit Geochemistry, Institute of Geochemistry, Chinese Academy of Sciences, 99th Linchengxi Road, Guiyang, Guizhou Province, China.
E-mail addresses: lingkunyue@mail.gyig.ac.cn (K.-Y. Ling), zhangzhengwei@vip.gyig.ac.cn (Z.-W. Zhang), wenhanjie@vip.gyig.ac.cn (H.-J. Wen).

https://doi.org/10.1016/j.oregeorev.2020.103325
Received 25 April 2019; Received in revised form 22 November 2019; Accepted 9 January 2020
Available online 18 January 2020
0169-1368/

LA–ICP–MS. Additionally, obtained reliable data from in-situ LA–ICP–MS study of the fine-grained minerals in sedimentary rock is difficult because the analysis objects are complex mineral aggregates and amorphous materials instead of a single mineral crystal. In recent years, LA methods were successfully applied to non-single mineral analysis. For instance, Konhauser et al. (2009) used LA and solution (whole-rock digestion) methods to analyze banded iron formation (BIF) samples; analysis results showed strong correspondence during the reconstruction of Ni/Fe ratios through time. Baldwin et al. (2011) successfully applied the LA method to analyze the trace element composition of chert micro-bands. In order to examine the analytical artifacts resulting from differences in in-situ laser ablation versus solution analyses, Robbins et al. (2019) systematically compared the LA data and solution values in BIF. The results showed that the LA data were nearly similar to the solution data. The preceding research achievements indicate that LA provides an effective method for sedimentary rocks and micro-sampling analysis.

In bauxite research, only a few LA–ICP–MS applications focused on detrital zircon U–Pb dating and Hf–O isotopic studies (Deng et al., 2010; Wang et al., 2010, 2016, 2018; Gu et al., 2013; Zhao et al., 2013; Huang et al., 2014; Yu et al., 2014a, 2016; Hou et al., 2017; Yang et al., 2018), which were used to investigate the genesis, provenance, and tectonic evolution of bauxite deposits. In addition, LA–ICP-MS was successfully applied to a pyrite trace element study on bauxite from Guangxi, China (Liu et al., 2017) because the pyrites showed either coarse-grained and euhedral or framboidal shapes with chemical purity, and therefore could be treated as a single crystal. However, the anion composition (i.e., OH^-) cannot be analysis by LA–ICP–MS, so that hydrous minerals such as diaspore, boehmite, kaolinite, illite, which may be the main host minerals of element Li–Ga–V–REE in bauxite, has never been studied by in-situ method. One interesting study is that by Chen et al. (2014), which had successfully accurately analyzed the major and trace elements of hydrous silicate minerals hornblende, epidote, tourmaline, and tremolite. The total content of the volatile components in the hydrous silicate minerals was first calculated through mineral constant stoichiometry. The major and trace elements were quantified by calibrating against multiple reference materials combined with normalization of all oxides to the sum of 100% minus the total volatile components (TVC). The analyses results reveal that major elements matched the results of electron microprobe analyses generally within 5% of uncertainty, whereas the trace elements were consistent with the results of solution–ICP–MS analysis combined with micro-sampling within generally 10% uncertainty for trace and REE elements. The above analyses shed light on the use of the in-situ method to investigate the trace element concentrations in the hydrous minerals in bauxites. Therefore, in this study, the LA–ICP–MS was applied to the research on aluminum oxide mineral and clay mineral aggregates try to reveal the main host minerals of Li, Ga, V, and REEs in Carboniferous karstic bauxites in southwest China.

2. Geological background and geological features

2.1. Geological background

The Carboniferous karstic bauxite, which is mainly located in central Guizhou Province in SW China, is typically characterized as global karstic bauxite and is the key exploration areas for important mineral resources in the country. The research area lies in the north Guizhou anticline in the southern margin of the Yangtze Plate (Fig. 1; Guizhou Bureau of Geology and Mineral Resources, 1987). During the early Paleozoic, the Guizhou area was situated within a coastal shallow marine environment (Rong et al., 2011; Chen et al., 2012). Since the late Ordovician, the central Guizhou was uplifted forming the central Guizhou Oldland, which constitutes one part of the ancient Upper Yangtze Land. Conversely, the southern and southwestern regions of Guizhou became a sedimentary basin (Fig. 1; Gao et al., 1992; Rong et al., 2011). This period was followed by 100 Ma of weathering and peneplanation, which resulted in the absence of Devonian, Silurian, and part of Ordovician strata in the central Guizhou region. These processes also formed quasi-lysogenic landforms, which included several karst depressions and basins that favored bauxite sedimentation (Fig. 1; Gao et al., 1992). During the Early Carboniferous, bauxite precursor rocks experienced weathering, deposition, and diagenesis processes and formed the Carboniferous Jiujialu Formation Al-bearing rock series mainly in the Qingzhen–Xiuwen and Xifeng–Zunyi karst basins (Fig. 1; Gao et al., 1992; Guizhou Bureau of Geology and Mineral Resources, 1987).

2.2. Geological features

Since the Yunwushan deposit was first discovered in 1941, more than 40 bauxite deposits, including the Xiaoshanba, Lindai, Yunwushan, and Houcao deposits in central Guizhou province have been discovered, with reserves exceeding 100 million tons (Figs. 1 and 2; Gao et al., 1992; Guizhou Department of Land and Resource, 2012). The bauxite deposits in Central Guizhou Province are controlled by the Central Guizhou anticlinorium and Ziyun–Yadu (ZY) and Puding–Guiyang–Huangping (PGH) faults, which strictly limited the distribution of the central Guizhou bauxite to the southern anticlinorium, northern PGH fault, and eastern ZY Fault (Fig. 1; Gao et al., 1992). The Xifeng–Zunyi ore belt is located in the northern limb of the anticlinorium, whereas the Qingzhen–Xiuwen ore belt is located in the southern limb (Gao et al., 1992; Fig. 1).

The exposed rock in the research area is primarily carbonate. The overall regional structure has a north-northeast (NNE) strike with two main fault orientations: northeast (NE) and NNE (Fig. 2). The ore body is hosted by the Lower Carboniferous Jiujialu Formation which displays unconformable contacts with the underlying lithologies (Fig. 3a, d). The underlying stratum from SW to NE includes the Lower Cambrian Qingxudong Formation dolomite, Middle Cambrian Gaotai and Shilengshui Formation dolomite, Middle and Upper Cambrian Loushanguan Group dolomite, and Lower Ordovian Tongzi to Meitan Formation dolomite and argillaceous rocks (Figs. 1–3; Bárdossy, 1982; Ling et al., 2017). The Jiujialu Formation is usually associated with carbonaceous rocks/coal seams and ferruginous rocks/iron ores with thickness in the range of 2–20 m (average of 8 m) (Fig. 3a–c, and e): (1) the upper segment that consists of coal layers comprising clay stone and black carbonaceous shale with the thickness ranging from 0.5 to 5 m (Fig. 3b); (2) the middle segment comprising bauxite layers with thickness in the range of 1–20 m (generally 5–10 m) (Fig. 3a and b); and (3) the lower segment comprising iron layers, which are primarily composed of red, steel gray, or dark ferruginous clay and iron rock with the thickness ranging from 0 to 6 m (Fig. 3c and e).

3. Sampling and analytical methods

All samples were collected from outcrops and open pits in the Xiaoshanba (XSB/XSB4), Lindai (LD/LD2), Yunwushan (YWS), and Houchao (HC) bauxite deposits, central Guizhou Province, southwest China (Figs. 2 and 3). The polished thin sections were prepared for Scanning Electron Microscope equipped with an Energy Dispersive Spectrometer (SEM-EDS) and LA-ICP-MS analyses. The former was conducted using a Thermo Scientific Scios DualBeam SEM-EDS at Institute of Geochemistry, Chinese Academy of Sciences (IGCAS).

In-situ analyses of bauxite samples were conducted using an Agilent 7900 LA–ICP–MS device equipped with a GeoLasPro 193 nm laser source at the State Key Laboratory of Ore Deposit Geochemistry, Institute of Geochemistry, Chinese Academy of Sciences (SKLODG-IGCAS). Operating conditions were as follows: 44 μm spot size, 5 Hz, and each analysis incorporates an approximately 20–30 s background acquisition (gas blank) followed by 50 s data acquisition from the sample. Multiple analyses of international standards NIST SRM 610 and NIST SRM 612

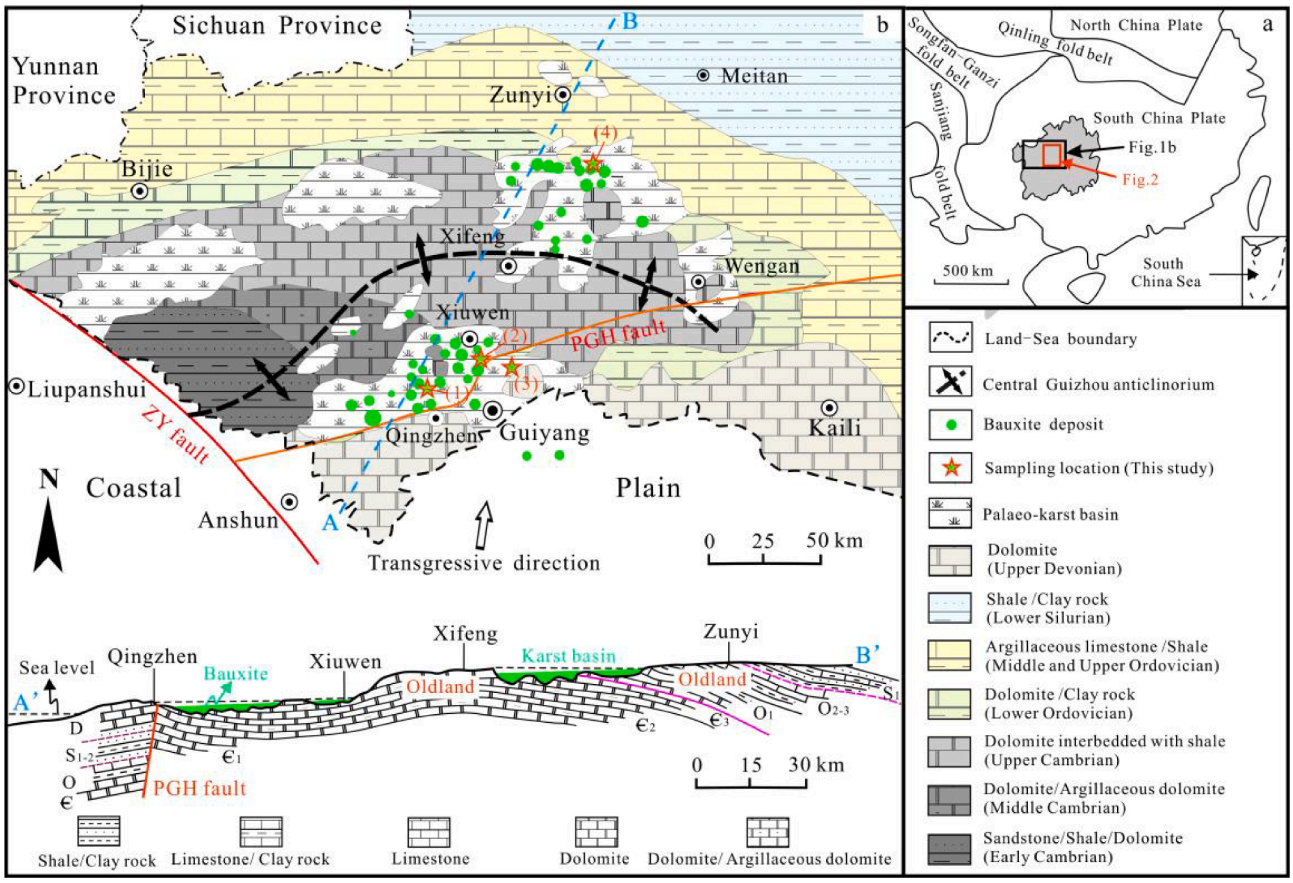

Fig. 1. (a) Inset map of the South China Plate showing the location of the research area. (b) Paleogeography and cross-section map of Lower Carboniferous Jiujialu Formation, central Guizhou province, SW China (modified from Gao et al., 1992). ZY fault: the Ziyun-Yadu fault; PGH fault: the Puding-Guiyang-Huangping fault. (1) Lindai deposit, (2) Xiaoshanba deposit, (3) Yunwushan deposit, and (4) Houcao deposit.

were used as calibration points and to constrain methodological error. All element data used for standardization were obtained from GEOREM (http://georem.mpch-mainz.gwdg.de/). Laser ablation data were processed using the ICPMSDataCal combined with normalization of all oxides to the sum of 100% minus the TVC of the chemical formula (Liu et al., 2008; Liu et al., 2010; Chen et al., 2014), i.e., diaspore/boehmite (AlO(OH); TVC = 15 wt%), kaolinite (Al_4 $[Si_4O_{10}](OH)_8$; TVC = 13.9 wt %), and illite ($KAl_2[(Si,Al)_4O_{10}](OH)_2{\cdot}nH_2O$; TVC = average 8.5 wt%) (Pan et al., 2006). The analytical and data procedures are detailed in Liu et al. (2008) and Chen et al. (2011, 2014). The data list in Table 1, which will be used for analysis and discussion later, shows the elements with relatively high content and stable signals of LA–ICP–MS, including Al_2O_3, SiO_2, FeO, MgO, P_2O_5, K_2O, TiO_2, Li, Ga, V, Sr, Zr, and ΣREE + Y (Fig. 4).

The major element abundances of whole-rock samples are checked by X-ray fluorescence (XRF) techniques (PANalytical, AXIOS-PW4400). The sample was crushed to 200 mesh using a mortar, and then a 0.7 g sample was weighted and a 7 g composite flux ($Li_2B_4O_7$:$LiBO_2$:LiF = 4.5:1:0.4) was added to platinum crucible before being mixed. The sample was heated at 1150 °C in a melting machine until it melted to liquid, and then analyzed by XRF before cooling and solidifying. The trace and REE abundances were analyzed through whole-rock solution–ICP–MS techniques (PlasmaQuant MS Elite). The ICP–MS measurements were quality controlled using international standard samples OU-6, AMH-1, and GBPG-1 (Potts et al., 2000, 2001; Thompson et al., 1999), and the relative standard deviation (RSD) was better than 10%. The detailed analytical procedures were described by Franzini et al. (1972) and Qi et al. (2000). The analyses of major, trace, and REE elements were accomplished at SKLODG-IGCAS and the results are summarized in Table 2.

The mineral components were analyzed at SKLODG-IGCAS by X-ray diffraction (XRD; Panalytical Empyream) equipped with PIXcel3D area detector, operating under the following conditions: at 40 kV and 40 mA. The XRD measurements were monitored by the instrument standard Cu Kα target, and semi-quantitatively calculated by the K value method (Table 3; Mordberg et al., 2000).

4. Results

4.1. Texture and mineralogy

Bauxite commonly consists of clastic, pisolitic/oolitic, and compact ores in the Carboniferous Jiujialu Formation, central Guizhou Province, southwest China (Fig. 5a–c). The clastic bauxite usually has off-white or ash-black color and exhibits clastic texture (Fig. 5a). The pisolitic/oolitic bauxite is commonly gray and characterized by pisolitic/oolitic texture (Fig. 5b). The compact bauxite is slippery and exhibits pelitomorphic texture (Fig. 5c).

The SEM analyses of the bauxite samples showed similar mineral compositions to other bauxites around the world (Mongelli, 1997; Laskou and Economou-Eliopoulos, 2013; Liu et al., 2012; Wang et al., 2012; Boni et al., 2013; Mongelli et al., 2014), which mainly comprise diaspore and boehmite, followed by kaolinite, illite, smectite, and a small amount of iron-bearing minerals and accessory minerals such as anatase/rutile and zircon (Fig. 5d–i). The diaspore/boehmite particles (2–10 μm) in clastic ore commonly have hypautomorphic crystal structures and exhibit short prismatic or platy shapes (Fig. 5d and h), whereas those in compact bauxites have xenomorphic crystal texture with fine particles (commonly less than 1 μm) (Fig. 5f). The pisolitic/oolitic baxutie was comprised of matrix and randomly distributed pisolitic (1–10 mm) and/or oolitic (0.1–1 mm) particles (Fig. 5e). The

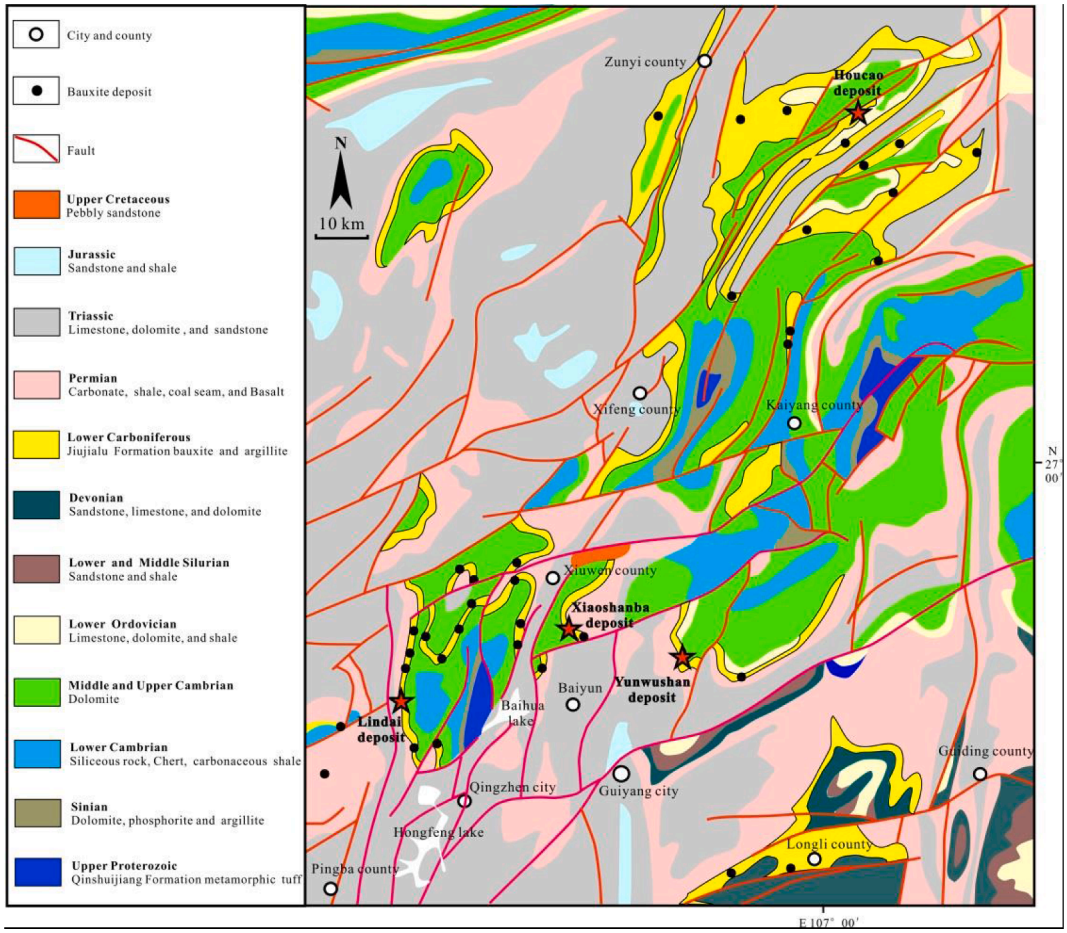

Fig. 2. Geological features of the central Guizhou bauxite, SW China (after the 1:200,000 map of geological and mineral resources, P. R. China, 1969).

chemical composition of pisolite/oolite was mainly aluminum oxide.

In the Xiaoshanba deposit, the chlorite, kaolinite, and an iron rocks underlying the bauxite ores were founded (Fig. 3c). The XRD results revealed that chlorite rocks primarily comprise chlorite. Iron rock comprises siderite, chlorite, and hematite. Kaolinite rocks comprise kaolinite and a small amount of anatase (Table 3).

4.2. In-situ geochemistry composition

LA–ICP–MS analyses showed that the main chemical constituent in diaspore/boehmite aggregate was Al_2O_3, which ranged from 79.5 to 83.7 wt%, with an average of 81.8 wt%. Other major elements SiO_2, TiO_2, FeO, MgO, P_2O_5, and K_2O were mostly less than 3 wt%, with an average concentration of 1.12, 1.06, 0.48, 0.04, 0.04, and 0.05 wt%, respectively (Table 1). Diaspore/boehmite has low Li (average 13.1 ppm) and ΣREE + Y (average 68.2 ppm), medium V (average 294 ppm), but high Ga and Zr concentrations (Table 1). Ga ranged from 98.6 to 409 ppm, with an average of 201 ppm, whereas Zr concentration varied widely, from 2.91 to 1781 ppm (average of 221 ppm).

The main chemical constituents of kaolinite aggregates were Al_2O_3 and SiO_2 with concentrations ranging from 40.9 to 55.5 wt% (average of 46.3 wt%) and from 24 to 40.3 wt% (average of 35.1 wt%), respectively. The average concentrations of TiO_2, FeO, MgO, P_2O_5, and K_2O contents were 1.91, 0.67, 0.69, 0.07, and 0.76, respectively (Table 1). Low Ga (average of 44.8 ppm); medium V (average of 157 ppm); and high Li, Zr, and ΣREE + Y concentrations in kaolinite aggregates (Table 1) were observed. Li ranged from 560 to 1625 ppm (average of 1508 ppm), whereas Zr and ΣREE + Y ranged from 89.2 to 696 ppm (average of 347 ppm) and from 64.8 to 1607 ppm (average of 281 ppm), respectively.

The main chemical constituents in illite aggregates were Al_2O_3, SiO_2, and K_2O with contents respectively ranging from 33.8 to 52.8 wt % (average of 43.4 wt%), from 32.2 to 43.7 wt% (average of 35.7 wt%), and from 5.55 to 8.1 wt% (average of 6.99 wt%). The trace elements of illite aggregates had characteristics similar to those in kaolinite aggregates, with low Ga (average 89.2 of ppm), medium V (average of 329 ppm) and ΣREE + Y (average of 68.2 ppm), and high Li, Zr, and ΣREE + Y (average of 68.2 ppm) concentrations (Table 1). Li ranged from 23.2 to 1027 ppm, with an average of 545 ppm, whereas Zr and ΣREE + Y ranged from 283 to 734 ppm (average of 488 ppm) and from 115 to 521 ppm (average of 277 ppm), respectively.

4.3. Whole-rock geochemistry composition

According to the results of XRD and ICP–MS analyses, samples of XSB4-1, 2, 4, and 5 were chlorite rocks with high contents of Al_2O_3 (average of 22.1 wt%), SiO_2 (average of 23.2 wt%), Fe_2O_3 (average of 34.9 wt%), and MgO (average of 6.81 wt%), whereas the contents of other major elements were less than 1 wt% (Table 2). The highest trace element in chlorite rocks was V, with contents ranging from 739 to 981 ppm and, average of 861 ppm, followed by ΣREE + Y (average of 685 ppm), Zr (average of 244 ppm), Li (average of 210 ppm), and Ga (average of 24.1 ppm) (Table 2). Iron rock XSB4-3 showed higher Fe_2O_3 (62.9 wt%) contents but lower contents of all the other elements compared with the chlorite rock samples (Table 2).

The predominant chemical constituents of kaolinite rock samples (XSB4-6, 7, and 8) were Al_2O_3 and SiO_2, followed by TiO_2 (average of 2.13 wt%), Fe_2O_3 (average of 1.5 wt%), MgO (average of 0.62 wt%), K_2O (average of 0.24 wt%), P_2O_5 (average of 0.16 wt%), CaO (average of 0.06 wt%), and NaO (average of 0.03 wt%) (Table 2). Al_2O_3 and SiO_2

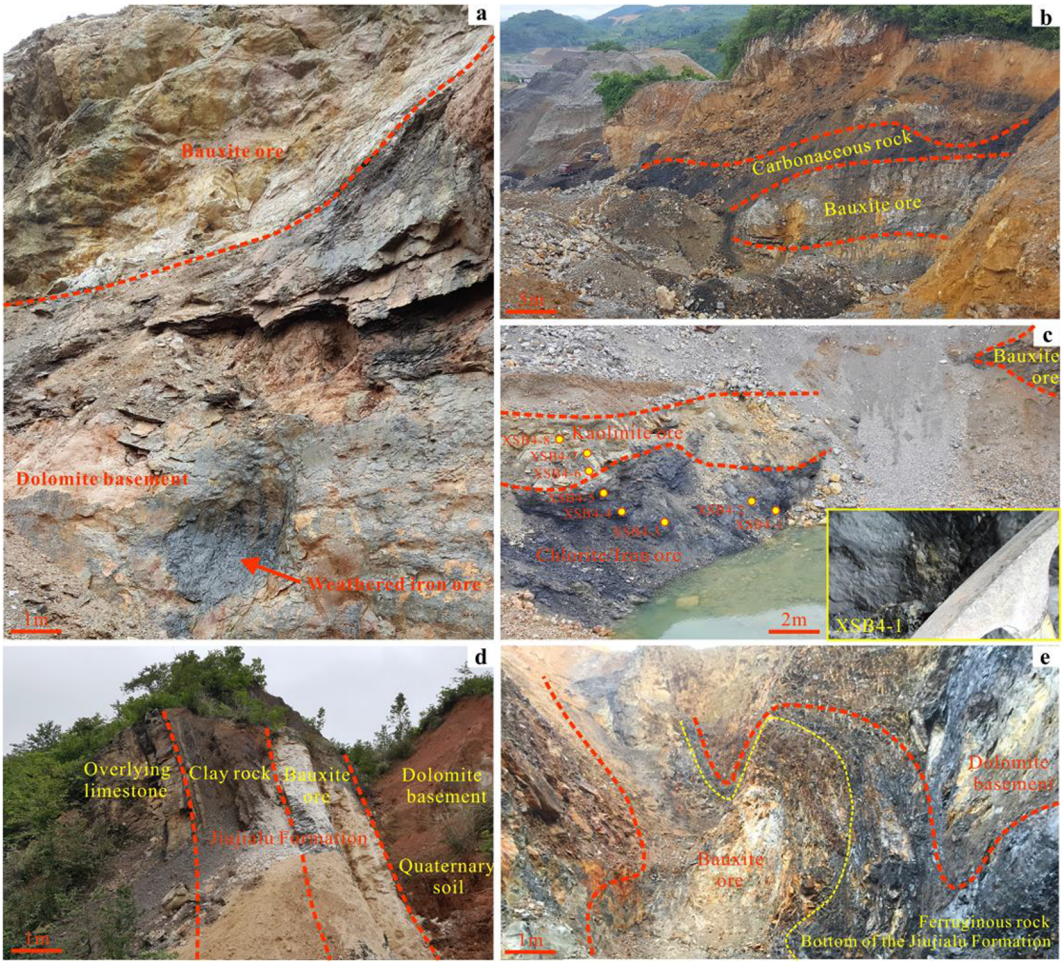

Fig. 3. Field photographs illustrating features of the central Guizhou bauxites, SW China. (a) Paleo-karst unconformity and overlying weathering iron ore/bauxite ore; (b) bauxite ore and overlying carbonaceous rock; (c) bauxite ore and underlying kaolinite rock/chlorite rock/iron ore; (d) Jiujialu Formation unconformable contacts with the overlying limestone and underlying dolomite; and (e) ferruginous rock and overlying bauxite ore.

contents ranged from 38.5 to 41.3 wt% (average of 39.5 wt%) and from 38.3 to 43.9 wt% (average of 42.1 wt%), respectively. ΣREE + Y was the highest trace element in kaolinite rocks, which ranged from 480 to 1290 ppm, with an average of 778 ppm, followed by Zr (average of 404 ppm), Li (average of 390 ppm), V (average of 111 ppm), and Ga (average of 12 ppm) (Table 2).

5. Discussions

5.1. Application of LA–ICP–MS to bauxite study

As mentioned previously, LA–ICP–MS analysis has been successfully applied to a geochemical study on non-single minerals and hydrous minerals. The analyses results revealed that the majority of element contents matched the results of EPMA and solution–ICP–MS analysis within generally 10% error (e.g., Konhauser et al., 2009; Baldwin et al., 2011; Chen et al., 2014; Robbins et al., 2019). However, the mineral composition of bauxite ores, particularly the accessory minerals that randomly distribute in bauxites, was complicated and various (Fig. 5), which may interfere with data reliability because the chemical component of these accessory minerals may influence the discussion and conclusion of the present study. Therefore, the main challenge of this study was eliminating the interference of accessory minerals. In this case, the laser spot selection is particularly important and based on the following rules: 1) the target mineral aggregates (i.e., diaspore/boehmite, kaolinite, or illite) should show simple and uniform mineral compositions, and 2) maldistribution and large particles of accessory minerals should be avoided (Fig. 4a–d). The LA–ICP–MS analysis showed signal stabilization and indicated successful laser spot selection (Fig. 4e–h). Furthermore, to ensure the reliability of data, this study used only major and selected trace elements (i.e., Li, Ga, V, and REEs + Y) with relatively high contents and stable LA-ICP-MS signals (Table 1; Fig. 4e–h).

To obtain further information on the candidate host minerals of Li, Ga, V, and REE + Y in bauxite, this study conducted element and mineral contents correlation analyses of Li–Ga–V–Zr–TiO_2–ΣREEs vs. Al_2O_3, V vs. Fe_2O_3, ΣREEs vs. P_2O_5, and Li–Ga vs. bauxite ore and clay minerals for bauxites from majority deposits that have been publicly reported around the world (Fig. 6). The significant positive correlations of TiO_2 vs. Al_2O_3 and Zr vs. Al_2O_3 indicated that a higher degree of chemical weathering of precursor rock, resulted in higher contents of Al_2O_3 and accessory minerals (such as rutile, anatase, zircon, and titanite; Fig. 6g and h) because these accessory minerals were generally inherited from the provenance rocks during ore-forming processes and ultimately enriched in the bauxites (Mordberg et al., 2001; Calagari and Abedini, 2007; Liu et al., 2013; Mongelli et al., 2014, 2016; Zamanian et al., 2016). The Li vs. Al_2O_3 bivariate plot showed a triangular shape, which indicated that the Li content increased with the improvement of Al_2O_3 content (because clay minerals improve with the decrease of quartz), peaked at approximately 50 wt%, and then decreased to almost zero (with the decrease of clay minerals and increase of Al oxide) (Fig. 6a). Combined with the positive and negative correlations of Li vs. bauxite ore mineral (i.e., diaspore/boehmite) and Li vs. clay mineral contents (Fig. 7c and d), respectively, implied that Li was mainly

Table 1
LA-ICP-MS analysis results of major (wt%), selected trace (ppm), and REE (ppm) element compositions from central Guizhou bauxites, SW China.

LA Spots	Minerals aggregate	Al_2O_3	SiO_2	FeO	MgO	P_2O_5	K_2O	TiO_2	Li	Ga	V	Zr	Y	La	Ce	Pr	Nd	Sm	Eu	Gd	Tb	Dy	Ho	Er	Tm	Yb	Lu	ΣREE + Y
YWS-4-01	Diaspore/boehmite	80.6	1.5	0.31	0.04	0.04	0.06	2.24	29.9	158	199	344	26.2	2.85	4.96	0.57	2.65	1.23	0.5	3.87	0.82	4.9	1.07	3.24	0.49	3.55	0.51	57.5
YWS-4-03	Diaspore/boehmite	82.5	1.65	0.39	0.04	0.05	0.03	0.17	21.9	128	228	60.9	5.1	1.26	2.33	0.28	1.32	0.47	0.11	0.6	0.13	0.9	0.2	0.61	0.08	0.68	0.09	14.2
YWS-4-04	Diaspore/boehmite	82.2	1.87	0.41	0.06	0.04	0.07	0.24	45.5	128	228	65.4	5.22	1.62	2.93	0.38	1.37	0.51	0.13	0.89	0.13	1.01	0.19	0.65	0.08	0.56	0.08	15.8
YWS-4-06	Diaspore/boehmite	80.7	2.58	0.19	0.05	0.05	0.07	1.16	55.1	122	109	248	19.1	5.82	10.5	1.08	5.16	1.49	0.4	2.42	0.45	3.57	0.82	2.26	0.42	2.95	0.43	56.9
YWS-4-10	Diaspore/boehmite	82.6	0.68	0.42	0.02	0.03	0	0.98	2.09	191	230	93.3	11.3	1.2	2.28	0.28	0.92	0.74	0.29	2.09	0.33	1.80	0.39	0.93	0.14	1	0.12	23.8
YWS-9-01	Diaspore/boehmite	82.7	0.76	0.53	0.04	0.03	0	0.77	1.66	296	285	88.4	17.3	0.42	0.67	0.1	0.83	1.64	0.42	3.06	0.50	3.08	0.49	1.31	0.20	1.26	0.2	31.5
YWS-9-02	Diaspore/boehmite	82.2	1.07	0.52	0.04	0.02	0.01	0.94	1.75	246	273	151	34.9	0.43	0.9	0.14	0.87	1.83	0.46	4.64	0.81	5.83	1.1	3.19	0.45	3.23	0.44	59.3
YWS-9-03	Diaspore/boehmite	82.2	0.86	0.53	0.03	0.03	0	1.09	1.07	212	280	238	18.4	0.55	0.96	0.14	1.05	1.50	0.49	3.34	0.62	3.53	0.59	1.74	0.23	1.41	0.23	34.8
YWS-9-04	Diaspore/boehmite	81.9	0.93	0.5	0.03	0.03	0	1.42	0.78	235	274	217	22.6	0.49	0.95	0.16	0.88	1.72	0.58	3.84	0.61	4.65	0.73	2.32	0.36	2.53	0.33	42.7
YWS-9-05	Diaspore/boehmite	81.5	1.14	0.56	0.04	0.03	0	1.53	0.82	159	255	229	21.8	1.02	2.1	0.26	1.22	1.26	0.49	3.05	0.64	3.68	0.71	2.15	0.34	2.54	0.43	41.7
YWS-9-06	Diaspore/boehmite	81.3	1.37	0.5	0.04	0.04	0	1.33	0.94	172	259	1781	62.3	0.54	1.34	0.17	1.16	2.12	0.81	6.23	1.24	8.98	1.94	7.06	1.51	13.59	2.18	111
YWS-9-09	Diaspore/boehmite	82.9	1.15	0.36	0.06	0.03	0.06	0.27	15.8	265	347	37.2	6.77	0.81	1.6	0.21	1.03	0.68	0.17	1.28	0.17	1.06	0.21	0.54	0.07	0.48	0.09	15.2
YWS-9-1-02	Diaspore/boehmite	81.8	0.56	0.37	0.03	0.03	0	1.23	0.67	138	250	262	25.6	4.52	7.25	0.76	3.50	1.74	0.37	2.9	0.73	4.97	0.86	2.42	0.39	3.14	0.45	59.6
YWS-9-1-05	Diaspore/boehmite	83.7	0.75	0.2	0.06	0.03	0.03	0.02	7.82	149	394	2.91	1.43	0.12	0.25	0.04	0.20	0.23	0.03	0.28	0.05	0.29	0.04	0.16	0.02	0.08	0	3.24
YWS-9-1-07	Diaspore/boehmite	82.5	0.65	0.42	0.04	0.02	0.01	0.72	3.02	216	281	132	20.4	3.54	4.89	0.71	3.34	1.76	0.57	3.42	0.56	3.68	0.64	1.80	0.26	1.79	0.26	47.6
YWS-9-1-08	Diaspore/boehmite	82.1	0.46	0.37	0.05	0.03	0.04	1.01	3.18	145	258	247	23.4	4.53	6.84	0.99	3.98	1.31	0.41	2.92	0.66	4.05	0.77	2.22	0.33	2.51	0.34	55.3
YWS-9-1-09	Diaspore/boehmite	80.9	1.35	0.38	0.07	0.03	0.28	0.94	29.9	182	250	153	18.9	9.23	14.8	1.88	9.28	2.83	0.62	3.55	0.58	3.34	0.63	1.69	0.30	1.85	0.26	69.7
YWS-9-1-10	Diaspore/boehmite	82.2	0.55	0.37	0.04	0.04	0	0.94	1.16	164	243	231	24.5	11.33	18.1	2.38	9.8	2.81	0.77	3.72	0.64	4.38	0.84	2.58	0.42	2.80	0.38	85.4
HC-004-03	Diaspore/boehmite	82.4	0.85	0.93	0.04	0.06	0.01	0.44	1.19	299	667	48.6	3.35	2.01	3.97	0.4	1.73	0.26	0.08	0.44	0.11	0.62	0.12	0.38	0.05	0.39	0.05	14
HC-004-04	Diaspore/boehmite	81.2	1.22	1.06	0.05	0.06	0.16	0.91	6.95	327	572	59.8	4.76	3.35	6.84	0.83	3.51	0.73	0.19	0.95	0.14	1.14	0.17	0.59	0.08	0.56	0.08	23.9
HC-004-05	Diaspore/boehmite	79.5	1.59	0.82	0.05	0.06	0.28	2.32	10.5	273	532	184	12.2	6.95	13.6	1.65	6.64	1.44	0.31	1.69	0.35	2.37	0.44	1.52	0.21	1.71	0.24	51.3
HC-004-08	Diaspore/boehmite	81	1.26	0.45	0.03	0.06	0.18	1.66	0.75	268	367	189	11.9	0.32	1.84	0.33	1.93	0.84	0.27	1.48	0.3	2.36	0.45	1.25	0.17	1.47	0.23	25.1
HC-004-09	Diaspore/boehmite	82	0.6	0.55	0.03	0.05	0	1.41	0.51	264	426	202	11.3	0.25	1.38	0.28	1.7	0.82	0.22	1.31	0.33	1.94	0.44	1.2	0.23	1.44	0.23	23.1
XSB-4-04	Diaspore/boehmite	81.6	0.82	0.45	0.04	0.09	0	1.61	5.18	136	114	442	89	136	221	21.7	67.33	10.56	2.33	14	2.62	15.5	3.03	9.46	1.38	9.19	1.3	604
XSB-4-05	Diaspore/boehmite	80	3.04	0.47	0.1	0.04	0.05	1.09	76.8	116	102	157	52.3	29.9	32.9	4.8	15.8	3.84	1.11	8.68	1.48	9.74	1.87	4.96	0.61	4.34	0.58	173
LD-8-01	Diaspore/boehmite	81.5	0.82	–	0.04	0.03	0.02	0.18	25.4	409	580	12.7	74.6	0.73	1.91	0.33	2.83	6.05	2.68	17.64	2.83	17.7	3.16	7.75	0.94	6.91	1.03	147
YWS4-2-06	Diaspore/boehmite	80.9	1.95	0.31	0.04	0.04	0.11	1.45	36.3	190	164	189	20.4	4.11	6.29	0.7	2.55	1.33	0.44	3.27	0.64	3.85	0.8	2.24	0.29	2.33	0.31	49.6
YWS4-2-07	Diaspore/boehmite	82.7	0.35	0.37	0.03	0.03	0	1.33	0.81	195	181	188	20.9	0.83	1.58	0.15	1.06	1.08	0.47	3.39	0.59	3.79	0.64	2.01	0.26	1.62	0.3	38.6
YWS4-2-08	Diaspore/boehmite	81.9	0.71	0.73	0.03	0.04	0.01	1.34	0.42	140	260	226	15.1	3.45	5.29	0.63	3.12	1.05	0.23	1.84	0.4	2.71	0.55	1.66	0.27	1.75	0.26	38.3
YWS4-2-10	Diaspore/boehmite	82.5	0.68	0.41	0.02	0.06	0.01	1.12	3.62	98.6	210	144	11.3	4.01	5.99	0.72	2.54	0.89	0.24	2.1	0.34	2.24	0.43	1.19	0.19	1.61	0.19	34
Average		81.8	1.12	0.48	0.04	0.04	0.05	1.06	13.1	201	294	221	23.1	8.07	12.9	1.43	5.31	1.83	0.54	3.63	0.66	4.26	0.81	2.37	0.36	2.64	0.39	68.2
YWS-4-02	Kaolinite	44.9	36.9	0.38	0.52	0.03	0.54	2.41	875	36	167	494	29.1	12.3	21.2	2.17	8.25	2.51	0.57	3.34	0.68	5.06	1.14	3.7	0.66	4.86	0.71	96.3
YWS-4-05	Kaolinite	40.9	40	0.36	0.51	0.05	0.58	3.18	911	28.1	150	469	26.5	15.4	28	3.14	11.8	3.08	0.82	3.82	0.68	4.82	1.05	3.48	0.52	3.98	0.59	108
YWS-4-08	Kaolinite	56.7	24	0.46	0.41	0.07	0.45	3.48	560	66.4	234	696	29.9	20.7	34.2	4.26	15.4	3.63	0.88	4.17	0.81	5.79	1.08	3.89	0.68	5.13	0.78	131
YWS-4-09	Kaolinite	44	38.5	0.49	0.73	0.08	0.85	0.89	1055	36.2	166	162	10.5	29.5	52.1	5.92	21.12	4.61	0.9	2.71	0.3	2.04	0.4	1.2	0.17	1.54	0.22	133
XSB-4-01	Kaolinite	52.5	30	0.98	0.82	0.04	0.39	0.95	1040	43.6	68	89.2	30.9	34.8	81.7	7.53	30.5	5.83	1.27	5.87	1.01	6.21	1.18	3	0.4	2.57	0.43	213
XSB-4-03	Kaolinite	42.8	35.1	0.96	0.94	0.24	0.64	4.14	1185	31.4	113	616	280	218	615	52.5	228	49.2	7.88	34.5	6.64	46	9.75	27.4	3.61	24.2	3.09	1607
XSB-4-06	Kaolinite	43	38.9	1.28	1.13	0.01	0.51	0.67	1625	21.2	61.8	127	16.5	10.7	17	1.77	6.31	1.33	0.3	2.09	0.46	3.06	0.72	1.94	0.29	2.08	0.29	64.8
LD-8-03	Kaolinite	40.2	38.8	1.1	0.86	0.08	2.08	2.06	1519	61.3	309	532	49.5	90.7	151	15.3	60.6	12.38	2.3	10.7	1.57	10.2	2.1	6.62	1.09	7.97	1.17	423
YWS4-2-04	Kaolinite	42.8	40.3	0.41	0.52	0.12	0.68	0.69	1086	40.7	134	186	9.23	32.5	57.3	6.52	24.1	5.4	0.93	2.99	0.27	1.83	0.33	1.23	0.19	1.32	0.23	144
YWS4-2-05	Kaolinite	55.5	27.5	0.45	0.5	0.06	0.66	0.99	820	86.1	163	195	14.4	18.7	33.4	3.78	15	3.48	0.64	2.68	0.44	2.58	0.55	1.57	0.25	2.21	0.31	100
YWS4-2-09	Kaolinite	45.9	36.4	0.52	0.59	0.03	0.67	1.51	959	41.1	160	250	15.1	11.7	20.7	2.23	8.75	2.02	0.45	2.18	0.36	2.7	0.58	1.91	0.29	2.64	0.32	72
Average		46.3	35.1	0.67	0.69	0.07	0.73	1.91	1058	44.8	157	347	46.6	45	101	9.56	39.1	8.5	1.54	6.82	1.2	8.22	1.72	5.08	0.74	5.32	0.74	281
YWS-9-08	Illite	33.8	40.4	3.84	0.85	0.14	7.58	3.71	1027	55.4	342	734	59.3	39.1	70.6	10.6	45.6	11.6	2.02	7.65	1.54	10.1	2.15	7.15	1.00	7.68	0.95	277
YWS-9-10	Illite	34.1	43.7	0.53	0.88	0.04	8.10	3.38	818	52.1	330	440	35.9	14.9	23.4	4.11	20.1	4.53	0.90	4.21	0.83	6.1	1.25	3.81	0.59	4.03	0.54	125
YWS-9-1-04	Illite	49.3	32.2	0.46	0.73	0.05	5.55	1.53	796	90.4	308	353	27.2	14.2	28	3.92	18	5.66	0.99	3.74	0.63	4.4	0.99	2.92	0.41	3.25	0.48	115
HC-004-06	Illite	52.8	29.3	0.47	0.24	0.13	6.28	1.55	23.2	130	348	629	47.9	113	224	22.9	71.9	9.72	1.65	5.96	1.07	7.40	1.62	5.58	0.87	6.79	0.98	521
LD2-1-02	Illite	47.1	32.8	0.45	0.29	0.08	7.44	2.82	61.4	118	316	283	18.6	76.7	155	16.6	55.6	7.38	1.17	3.86	0.57	3.63	0.74	2.05	0.3	2.4	0.35	345
Average		43.4	35.7	1.15	0.6	0.09	6.99	2.6	545	89.2	329	488	37.8	51.5	100	11.6	42.2	7.78	1.35	5.08	0.93	6.32	1.35	4.3	0.64	4.83	0.66	277
HC-004-01	Rutile/Anatase	4.5	2.01	0.06	0.03	0.02	0.6	92.6	0.41	19.5	84.5	211	10.9	0.16	0.96	0.21	1.4	0.55	0.14	0.93	0.24	2.11	0.43	1.53	0.21	1.71	0.26	10.8

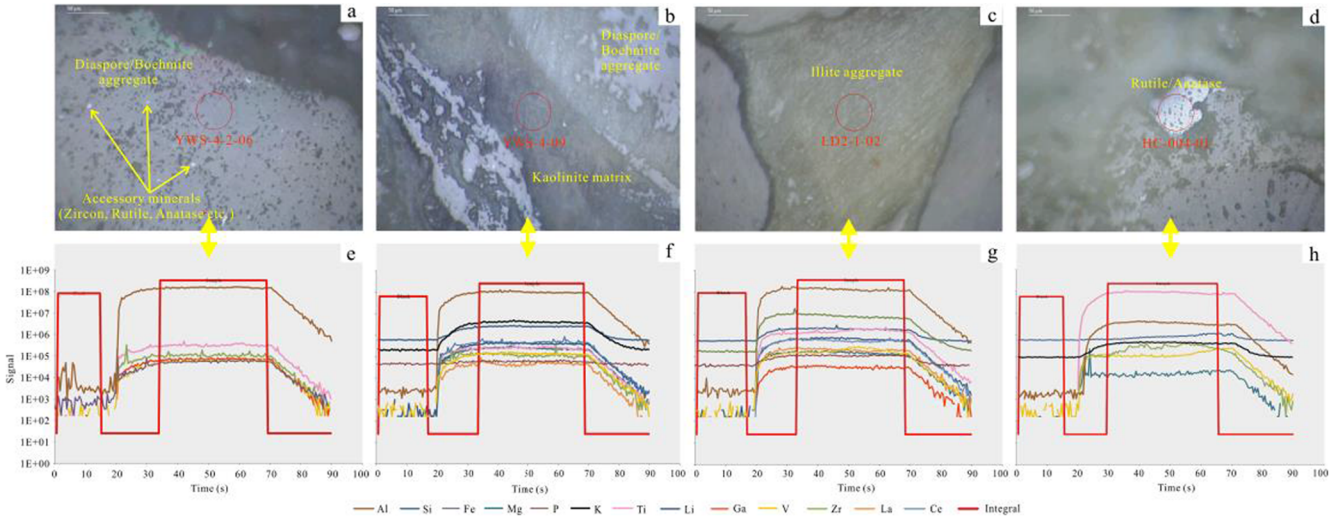

Fig. 4. (a–d) BSE images showing the Laser ablation spots, which are simple and uniform mineral compositions, and avoid maldistribution and large particles of accessory minerals; (e-h) LA-ICP-MS analysis shows signs stabilization, indicate a successful spot selections.

enriched in clay minerals rather than accessory minerals (Karayigit et al., 2006; Wang et al. 2013; Yu et al., 2014b; Ling et al., 2018). The Al_2O_3 and bauxite ore mineral vs. Ga contents showed positive correlations, which combined with the negative correlation of clay minerals vs. Ga contents (Fig. 7a and b), revealed that diaspore/boehmite rather than accessory minerals were the main host minerals of Ga. This result was consistent with previous conclusions that Ga always isomorphically substitutes Al in aluminum oxides, i.e., gibbsite, diaspore and boehmite in bauxite (Tang et al., 2002; Lu et al., 2009). The occurrence of V in bauxite was not very clear (Mordberg et al., 2001; Mongelli et al., 2014). The negative correlation of V vs. Al_2O_3 contents but positive correlation of Zr and TiO_2 vs. Al_2O_3 contents (Fig. 6c, g, and h) implies that Al oxides and accessory minerals may not be the main host minerals of V. Previous studies have shown that REEs + Y mainly absorbed on clay minerals, phosphate minerals, and within REE minerals such as bastnäsite, cerianite, xenotime, and monazite in bauxites (e.g., Braun et al., 1993; Condie, 1993; Pokrovsky et al., 2006; Esmaeily et al., 2010; Wang et al., 2010; Gu et al., 2013; Mongelli et al., 2014; Zamanian et al., 2016). Additionally, accessory minerals such as rutile and anatase play an important role in the concentration of REEs + Y during bauxite mineralization (Karadağ et al., 2009; Esmaeily et al., 2010; Zamanian et al., 2016). In this study, ΣREEs vs. Al_2O_3 bivariate plot (Fig. 6e) showed two spikes of ΣREEs contents within the scope of 20–40 wt% and 50–75 wt% of Al_2O_3 contents, which implies the presence of REE-independent minerals. Furthermore, the positive correlation of ΣREEs vs. P_2O_5 contents (Fig. 6f) provides another evidence that REE-independent minerals, such as monazite (Ce, La, Nd) PO_4, may be the main host minerals of REEs. In addition, another phosphate mineral apatite was another candidate mineral because Ca can be easily isomorphically substituted by REEs (Wu et al., 2017; Takaya et al., 2018).

In general, accessory mineral particles in bauxites were not the main host minerals of Li, Ga, V, and REE + Y. Thus, the trace element content analyses by LA–ICP–MS in this study can represent the contents of Al oxides and/or clay minerals. However, this study cannot exclude interference from other clay minerals. For instance, the analysis of kaolinite aggregate showed that Li content was very high (Table 1) but cannot conclude that Li was rich in kaolinite because the aggregate may contain other fine mineral particles (Fig. 5g–i). Drawing the conclusion in this study should involve combining other evidence, such as element correlation (see Fig. 8). Only in this manner can LA–ICP–MS be used as an effective method to investigate the main host minerals of Li, Ga, V, and REE + Y in bauxite. According to the above rules, the LA–ICP–MS results showed similar characteristics of bivariate plots of selected elements (Fig. 8; such as positive correlation of MgO vs. Li, FeO vs. V, and P_2O_5 vs. ΣREE) to statistical results of whole-rock sample from global bauxites (Fig. 6). It offers another solid proof that LA–ICP–MS was successfully applied to karstic bauxite analysis in this study.

5.2. Host mineral of Li, Ga, V, and REEs

5.2.1. Host mineral of Li

As mentioned in the previous section, Li were mainly absorbed by clay minerals such as kaolinite, illite, and smectite in karstic bauxites (Karayigit et al., 2006; Wang et al. 2013; Ling et al., 2018). In this study, Li contents in kaolinite and illite aggregates (average of 1058 and 545 ppm, respectively) were much higher than those in diaspore/boehmite (average of 13.1 ppm) (Table 1), which implied that kaolinite and illite could be the candidate host minerals of Li. In addition, other fine clay mineral particles, such as smectite and chlorite mixed within kaolinite and illite aggregates, could be other candidates because smectite such as saponite which may be transformed by other coarse grained mineral had been discovered by SEM–EDS (Fig. 5f). The lower Li contents in whole-rock samples of chlorite (XSB4-1, 2, 4, and 5; average Li contents: 210 ppm) and kaolinite rocks (XSB4-6, 7, and 8; average Li contents: 390 ppm) from Xiaoshanba bauxite deposit (Fig. 3c; Table 2), combined with the positive and negative correlations of Li vs. MgO and Li vs. K_2O, respectively, and huge variation (more than 40 times) of Li content in illite aggregates, would suggest that Mg-rich mineral smectite instead of kaolinite and illite was the main Li host mineral in bauxite (Fig. 8a and b; Table 1). It has been demonstrated by previous research that smectite mineral crystal had a cation exchange layer (interlayer) that could absorb large amounts of Li ions (Pan et al., 2006). Additionally, sulfuric acid leaching experiment of bauxitic rock from the study area revealed that after calcined at 500–600 °C, 74% Li extracted via ion exchange instead of mineral dissolution because the stratified structures of clay minerals were not destroyed (Gu et al., 2020). As a consequence, the above results imply that Li was mainly incorporated into smectite interlayer in the Jiujialu Formation.

5.2.2. Host mineral of Ga

Ga contents in diaspore/boehmite aggregates (average of 201 ppm) were much higher than those in chlorite rocks (average of 24.1 ppm), kaolinite (average of 44.8 ppm), and illite aggregates (average of 89.2 ppm) (Table 1), which suggested that the diaspore/boehmite was the main host mineral of Ga. This result coincided with the findings of previous research and statistical studies of majority deposits around the

Table 2
Major (wt%), selected trace (ppm), and REE (ppm) element compositions of whole-rock samples from the Xiaoshanba bauxite deposit, central Guizhou Province, SW China.

Sample no.	lithology	Al_2O_3	SiO_2	FeO	CaO	Na_2O	K_2O	MgO	MnO	P_2O_5	TiO_2	LOI	Li	Ga	V	Zr
XSB4-1	Chlorite rock	21.6	23.4	38.8	0.13	0.06	–	5.41	0.01	0.12	0.93	9.27	129	23.8	981	204
XSB4-2	Chlorite rock	19.3	20.9	36.7	0.56	0.06	–	4.57	–	0.41	0.29	16.3	112	22.5	831	84.4
XSB4-3	Iron ore	5.56	6.76	62.9	1.82	0.08	–	2.94	0.18	0.29	0.15	18.6	19.7	8.16	695	33.5
XSB4-4	Chlorite rock	25.5	23.8	27	0.1	0.08	0.15	11.5	0.01	0.24	1.78	9.5	437	21.1	893	452
XSB4-5	Chlorite rock	21.8	24.8	37	0.14	0.08	0.27	5.8	0.01	0.15	0.92	8.42	164	29.2	739	234
Average		22.1	23.2	34.9	0.23	0.07	–	6.81	–	0.23	0.98	10.9	210	24.1	861	244
XSB4-6	Kaolinite rock	38.5	43.9	1.29	0.05	0.01	0.12	0.41	–	0.15	1.93	13.6	367	8.65	74.9	344
XSB4-7	Kaolinite rock	38.8	43.9	0.64	0.06	0.03	0.14	0.3	–	0.16	2	13.8	404	9.01	57.7	407
XSB4-8	Kaolinite rock	41.3	38.3	2.56	0.08	0.05	0.46	1.16	–	0.18	2.46	13.2	399	18.3	201	460
Average		39.5	42.1	1.5	0.06	0.03	0.24	0.62	–	0.16	2.13	13.5	390	12	111	404

Sample no.	Y	La	Ce	Pr	Nd	Sm	Eu	Gd	Tb	Dy	Ho	Er	Tm	Yb	Lu	ΣREE + Y
XSB4-1	285	58.8	150	14.4	69.3	18.5	5.88	42.8	6.1	38.2	7.89	21.3	2.96	17.7	2.72	741
XSB4-2	97.6	13.7	24	2.53	10.3	9.6	5.53	31.2	3.17	15.9	2.88	7.17	0.96	5.93	0.87	231
XSB4-3	59.7	7.26	19.2	2.11	10.9	7.75	3.61	18.5	1.77	8.88	1.62	4.02	0.51	3.03	0.46	149
XSB4-4	226	130	249	27.1	118	29.4	5.89	33.4	4.45	27.6	5.99	16.5	2.3	14.1	2.17	891
XSB4-5	389	64.3	145	14.8	73.4	22.4	6.2	43.2	6.71	44.6	10	27.2	3.84	23.4	3.61	877
Average	249	66.6	142	14.7	67.7	20	5.87	37.6	5.11	31.5	6.7	18.1	2.51	15.3	2.34	685
XSB4-6	11.2	108	226	20.5	89.6	9.67	1.18	5.6	0.65	2.65	0.53	1.93	0.27	1.91	0.28	480
XSB4-7	15.9	112	285	21.6	98.8	11.8	1.71	7.46	0.85	3.64	0.73	2.35	0.32	2.16	0.32	565
XSB4-8	44.3	32	581	55.6	199	29.2	4.4	19.5	2.39	11.1	2.08	6.51	0.92	5.99	0.88	1290
Average	23.8	183	364	32.6	129	16.9	2.43	10.8	1.3	5.78	1.11	3.59	0.5	3.36	0.49	775

Notes: “ – ” means not determined.

Table 3
Relative abundance (wt%) of minerals in selected samples from XRD.

Sample no.	Lithology	Major minerals (wt% > 15%)	Minlor minerals (wt% < 15%)
XSB4-1	Chlorite rock	Chlorite	
XSB4-2	Chlorite rock	Chlorite	Hematite
XSB4-3	Iron ore	Siderite, Chlorite, Hematite	
XSB4-4	Chlorite rock	Chlorite	Hematite
XSB4-5	Chlorite rock	Chlorite	Hematite
XSB4-6	Kaolinite rock	Kaolinite	Anatase
XSB4-7	Kaolinite rock	Kaolinite	Anatase
XSB4-8	Kaolinite rock	Kaolinite	Anatase, Diaspore

world (Figs. 6b and 7a; Tang et al., 2002; Lu et al., 2009). The similar ionic radius of Ga^{3+} (0.62 nm) and Al^{3+} (0.57 nm) means that Ga^{3+} could isomorphically substitute Al^{3+} in aluminum oxides, such as gibbsite, aluminosilicates, and particularly diaspore and boehmite (Tang et al., 2002; Lu et al., 2009). In addition, crystal chemical investigations revealed that Ga could easily isomorphically substitute Al in diaspore and boehmite, ultimately becoming enriched in bauxite ores during bauxite mineralization (Bárdossy and Aleva, 1990; Tang et al., 2001; Liu et al., 2013; Mongelli et al., 2014, 2016).

5.2.3. Host mineral of V

V is mainly used in the steel industry and is an important raw material for alloy smelting. V is also a dispersed element and associates abundantly in coal, bauxite, phosphorus deposits and others. V is enriching in bauxites and is one of the elements successfully extracted as a by-product of Al production (Mongelli, 1997; Mordberg et al., 2001; Calagari and Abedini, 2007; Wang et al., 2012; Hanilçi, 2013). In general, the occurrence of V in bauxite was sufficiently understood. EPMA and geochemistry studies suggested that Ti oxides played an important role in the accumulation of V (Lu et al., 2009; Mordberg et al., 2001; Mongelli et al., 2014). In this study, LA–ICP–MS analysis revealed a different result that rutile/anatase contained only 84.5 ppm of V (Table 1). Furthermore, the positive correlation of V vs. Fe_2O_3 contents in whole-rock samples (Fig. 6d) and diaspore/boehmite aggregates (Fig. 8c) implies that V was closely related to iron-bearing minerals mixing within bauxites. In addition, the V contents in chlorite rocks (average of 861 ppm) were much higher than those in kaolinite rocks (average of 111 ppm), kaolinite aggregates (average of 157 ppm), diaspore/boehmite aggregates (average of 294 ppm), and illite aggregates (average of 329 ppm) (Table 2), which would imply that chlorite was the mineral containing the highest V in bauxite. Furthermore, the sample XSB4-3 that mainly comprised of siderite and chlorite showed lower V (695 ppm) than chlorite rocks (ranging from 739 to 981 ppm, with an average of 861 ppm) and presenting further evidence that chlorite was the main host mineral of V (Tables 2 and 3). The Early Cambrian black-shale sequence in South China have spectacular metal contents including V, which mainly enriched in illite and chlorite through substitute Al and Fe in octahedral sites (e.g., Lehmann et al., 2016; Li, 2019). This implies that V was most likely incorporated into chlorite octahedral site in this study because Fe-rich chlorite rocks were

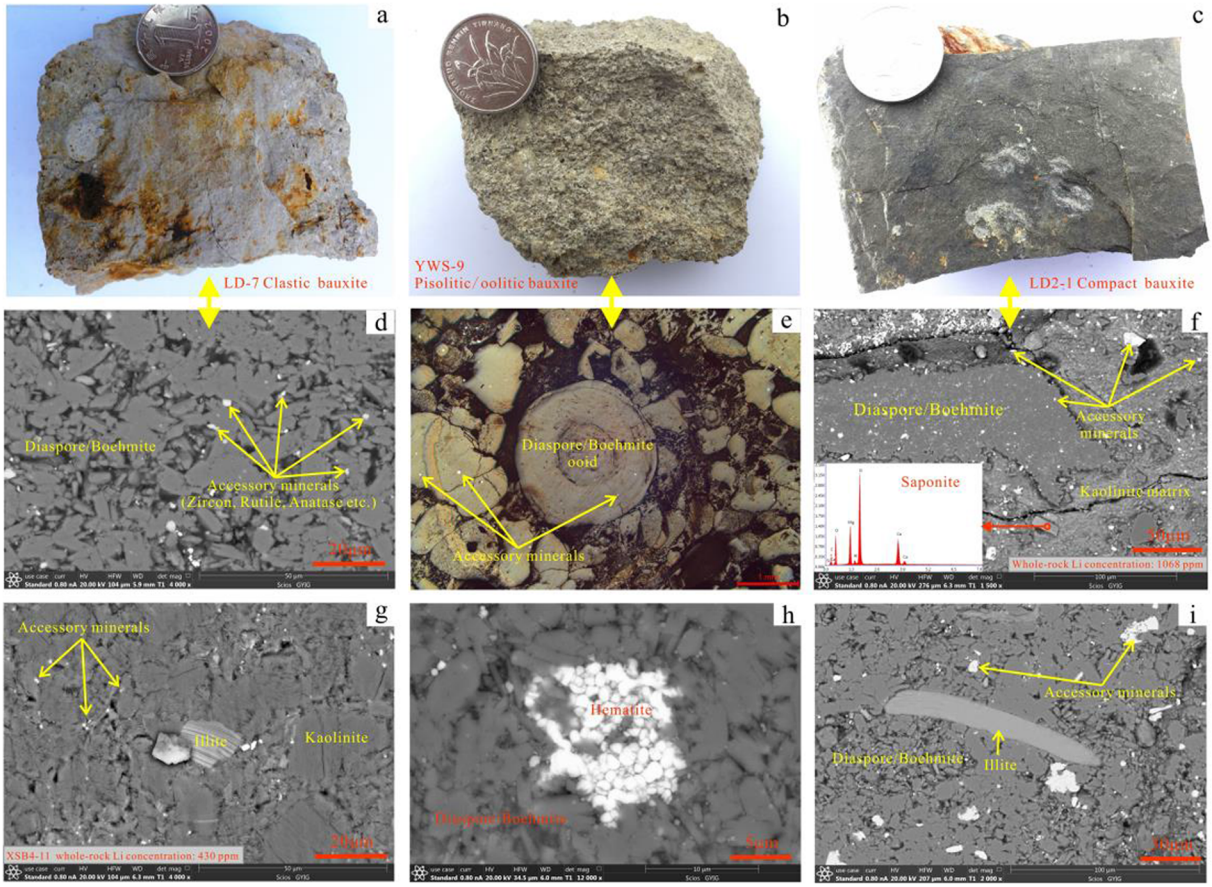

Fig. 5. Macro and backscattered electron (BSE) images of bauxite samples from central Guizhou bauxites. Specimen images of (a) the clastic bauxite, (b) the pisolitic/oolitic bauxite, and (c) the compact bauxite; BSE images of (d) the clastic bauxite; mineral compositions are dominated by short prismatic or platy shape (2–10 μm) diaspores/boehmites with minor accessory minerals of zircon/rutile/anatase. (e) The pisolitic/oolitic bauxite; comprise of matrix and randomly distributed pisolitic (1–10 mm) and/or oolitic (0.1–1 mm) particles. (f) The compact bauxite; diaspore/boehmite, kaolinite matrix, zircon, and rutile/anatase are coexisting. Smectite group mineral saponite $(Ca_{0.25}(Mg,Fe^{+2})_3(Si,Al)_4O_{10}(OH)_2{\cdot}4H_2O)$ is scattered within bauxite ore/clay rock.

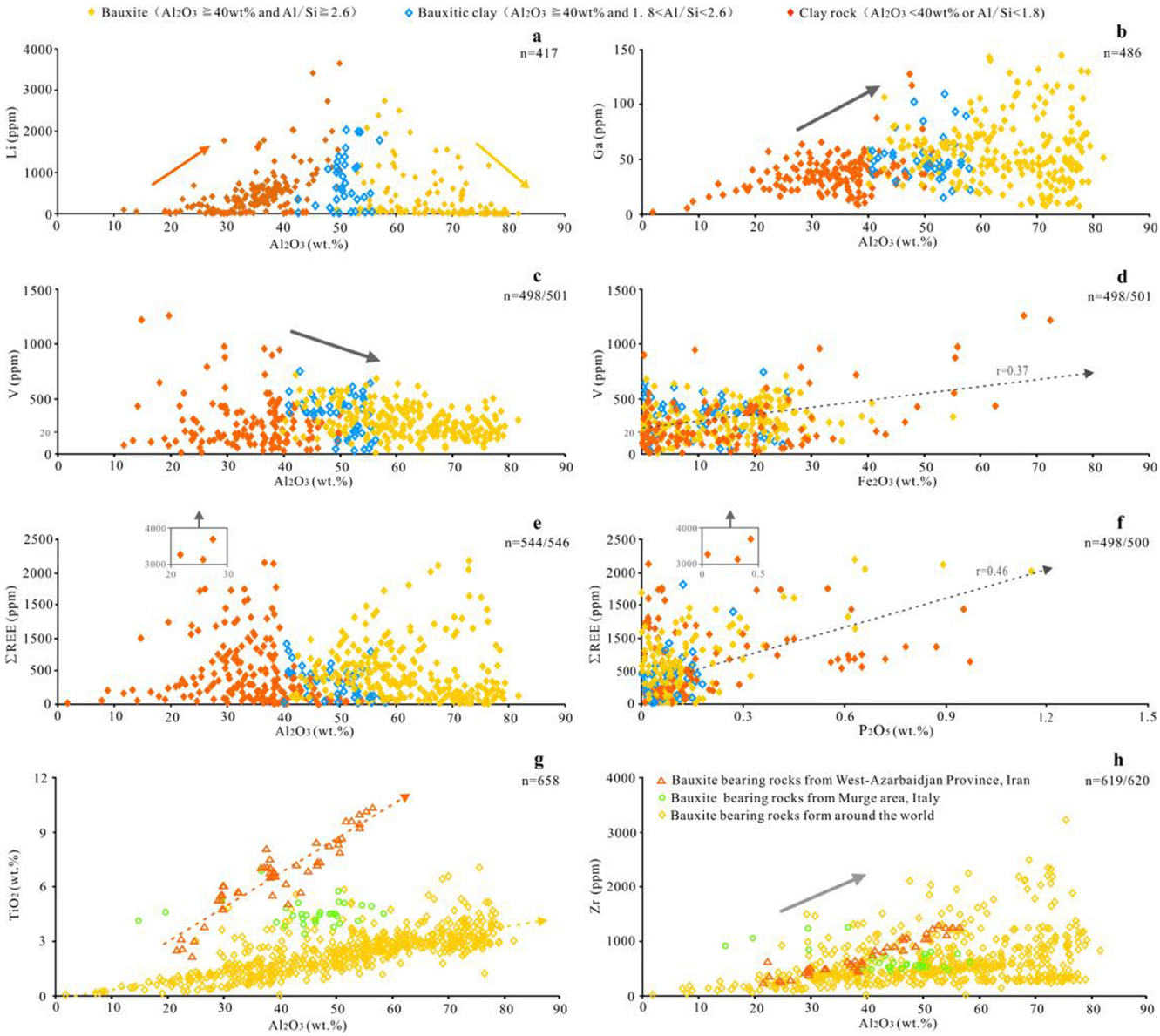

Fig. 6. Bivariate plots of Al_2O_3 vs. (a) Li, (b) Ga, (c) V, (e) ΣREE, (g) TiO_2, and (h) Zr, (d) Fe_2O_3 vs. V and (f) P_2O_5 vs. ΣREE. Data from majority deposits that have been publicly-reported around the world (Mongelli et al., 2014; Mordberg et al., 2000; Öztürk et al., 2002; Mameli et al., 2007; Ye et al., 2008; Deng et al., 2010; Boni et al., 2012; Zarasvandi et al., 2012; Wang et al., 2012, 2013, 2014; Hanilçi, 2013; Zhang et al., 2013; Li, 2013; Li et al., 2013; Liu et al., 2013, 2016; Abedini and Calagari, 2014; Huang et al., 2014; Yu et al., 2014b, 2016; Zamanian et al., 2016; Ahmadnejad et al., 2017; Hou et al., 2017; khosravi et al., 2017; Long et al., 2017; Yuste et al., 2017; Abedini et al., 2018; Weng et al., 2019). The West-Azarbaidjan Province, Iran and Murge area, Italy bauxites showed different Al_2O_3 vs. TiO_2 plots from others, due to its precursor rocks were mainly of magmatic rocks, which have higher titanium content.

formed in anoxic/suboxic environment, which similar to black-shale in South China (Han et al., 2018).

5.2.4. Host mineral of REEs

Previous studies have discovered many REE-independent minerals, including bastnäsite, parisite, cerianite, rhabdophane, and churchite in the karstic bauxites (Wang et al., 2010; Gu et al., 2013; Li et al., 2013; Liu et al., 2016; Radisinović et al., 2017). As mentioned above, the statistical studies of majority deposits around the world and LA–ICP–MS analysis results showed positive correlation of ΣREEs vs. P_2O_5 contents, thereby implying that REE-rich apatite and REE-independent minerals may be the main host minerals of REEs (Figs. 6f and 8d). In this study, numbers REE-bearing nano-particles were discovered by SEM–EDS (Fig. 9). According to the results of EDS analyses, these particles comprised Al oxide, aluminosilicate, and REE-independent minerals. The EDS analyses revealed that Ce and Nd, which were the most abundant REE in XSB4-14, were detected by SEM-EDS (Fig. 9), and the Ce and Nd contents ranged from 1.2 wt% to 1.9 wt% (average of 1.6 wt%) and from 1.8 wt%to 2.5 wt% (average of 2.2 wt%), respectively (Fig. 9). In addition, P (with an average of 1.4 wt% and 1.6 wt%) was detected by EDS, whereas Ca was not, thereby implying that the REE-bearing particle was monazite (Ce, La, Nd) PO_4 (Fig. 9), which is one of the richest REE-independent mineral in the Bayan Obo REE-Fe-Nb deposit, Inner Mongolia, North China (Yang et al., 2017; Liu et al., 2018).

6. Conclusions

LA–ICP–MS was successfully applied to hydrous mineral element geochemistry analysis within karstic bauxite samples based on the principle that laser ablation data were normalizatized in all oxides to the sum of 100% minus the TVC of the chemical formula. The analysis showed signal stabilization. The results exhibited that the

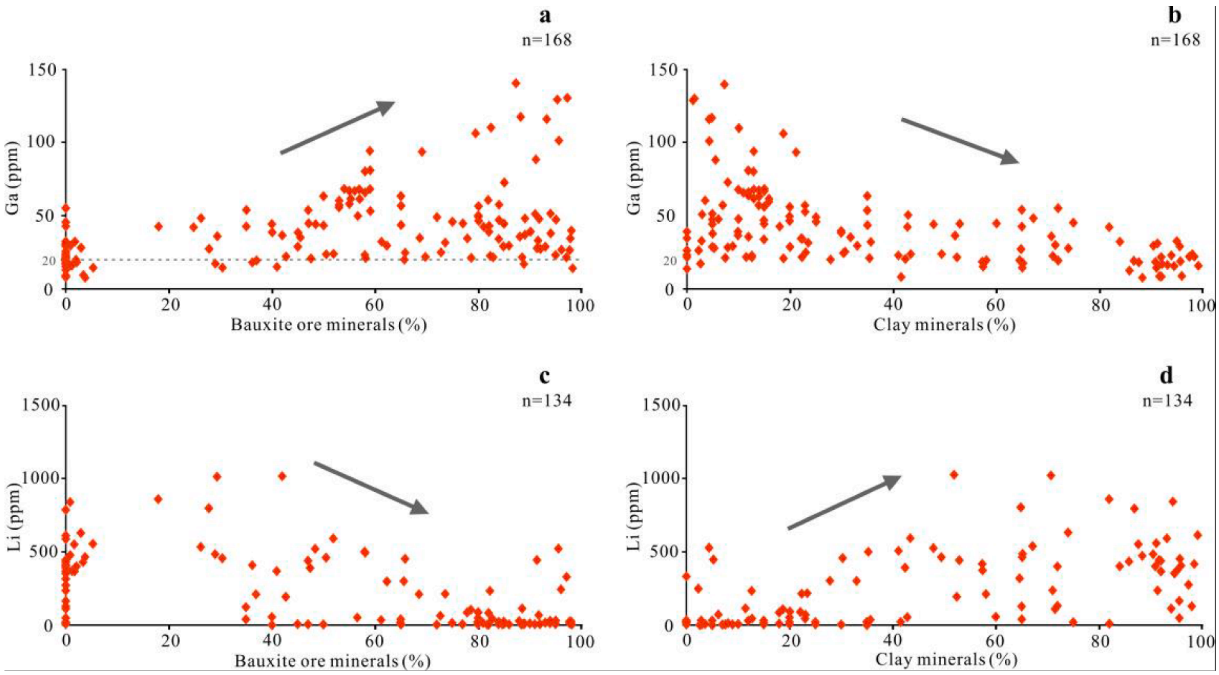

Fig. 7. Bivariate plots of bauxite minerals and clay minerals vs. (a-b) Ga and (c-d) Li, respectively. Data from publicly-reported bauxite deposits around the world (Mameli et al., 2007; Li, 2013; Liu et al., 2013; Mongelli et al., 2014; Ling et al., 2015, 2018; Long et al., 2018; Weng et al., 2019).

characteristics of bivariate plots of selected elements were similar to the statistical results of whole-rock samples from global bauxites, which indicate that the analysis data in this study were reliable instead of artificial in this study. This shed light on the use of the in-situ method to investigate the trace element concentrations in the hydrous minerals and sedimentary rocks.

Karstic bauxite throughout the world is rich in trace elements, which have the potential for comprehensive utilization as independent deposits or associated resources. This study revealed that smectite may be the main host minerals of Li. Furthermore, Ga was enriched in diaspore/boehmite, with contents ranged from 98.6 to 409 ppm (average of 201 ppm), V was mainly enriched in iron-bearing minerals particularly chlorite (ranging from 739 to 981 ppm with average of 861 ppm), and REE-independent minerals, such as monazite, were the main host minerals of REEs in Carboniferous karstic bauxite, SW China.

Declaration of Competing Interest

The authors declare that they have no known competing financial interests or personal relationships that could have appeared to influence the work reported in this paper.

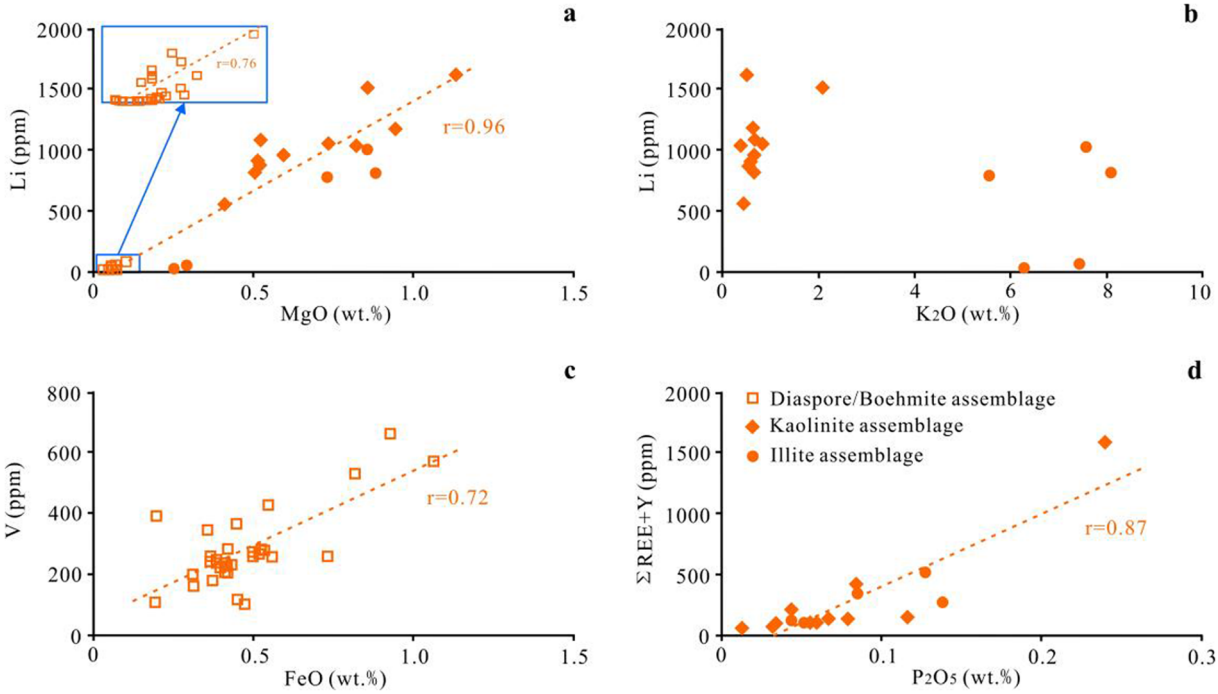

Fig. 8. Bivariate plots of (a) MgO vs. Li, (b) K_2O vs. Li, FeO vs. V, and P_2O_5 vs. ΣREE + Y. Data from LA-ICP-MS analysis, this study.

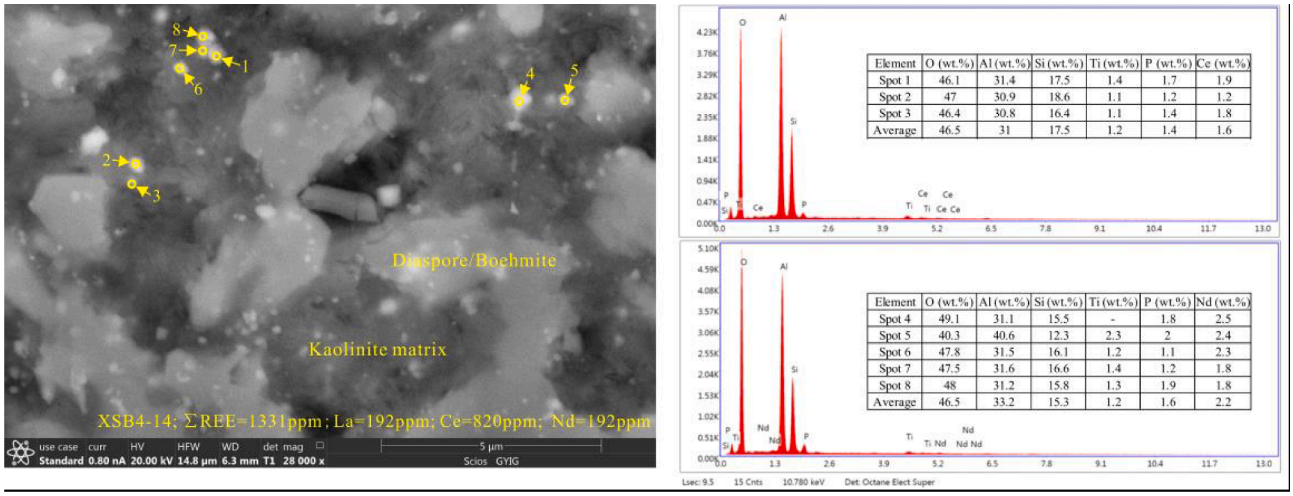

Fig. 9. BSE images of the sample XSB4-14 showing the existence of REE independent mineral monazite ((Ce, La, Nd) PO_4).

Acknowledgments

This study was financially supported by the National Key R&D Program of China (2017YFC0602503), the National Natural Science Foundation of China (41703052, U1812402, U1603245, and 41872085), the CAS "Light of West China" Program, and the Qian Sci & Tec Supporting Plan ([2019]1319). The authors would like to thank Dr. Cheng-Quan Wu, Yan-Wen Tang, and Bing Mo for their assistance on the LA-ICP-MS and SEM-EDS analysis.

Appendix A. Supplementary data

Supplementary data to this article can be found online at https://doi.org/10.1016/j.oregeorev.2020.103325.

References

Abedini, A., Calagari, A.A., 2014. REE geochemical characteristics of titanium-rich bauxites: the Permian Kanigorgeh horizon. NW Iran. Turkish J Earth Sci. 23, 513–532.
Abedini, A., Khosravi, M., Calagari, A.A., 2018. Geochemical characteristics of the Arbanos karst-type bauxite deposit, NW Iran: Implications for parental affinity and factors controlling the distribution of elements. J Geochem. Explor. 200, 249–265.
Ahmadnejad, F., Zamanian, H., Taghipour, B., Zarasvandi, A., Buccione, R., Salamab Ellahi, S., 2017. Mineralogical and geochemical evolution of the Bidgol bauxite deposit, Zagros Mountain Belt, Iran: Implications for ore genesis, rare earth elements fractionation and parental affinity. Ore Geol. Rev. 86, 755–783.
Baldwin, G.J., Thurston, P.C., Kamber, B.S., 2011. High-precision rare earth element, nickel, and chromium chemistry of chert microbands pre-screened with in-situ analysis. Chem. Geol. 285, 133–143.
Bárdossy, G., 1982. Karst bauxites, bauxite deposits on carbonate rocks. Developments in economic geology 14. Elsevier, Amsterdam, pp. 1–441.
Bárdossy, G., Aleva, G.J.J., 1990. Lateritic bauxites. Elsevier Scientific Publication, Amsterdam, pp. 624.
Boni, M., Reddy, S.M., Mondillo, N., Balassone, G., Taylor, R., 2012. A distant magmatic source for Cretaceous karst bauxites of southern Apennines (Italy), revealed through SHRIMP zircon age dating. Terranova 24, 326–332.
Boni, M., Rollinson, G., Mondillo, N., Balassone, G., Santoro, L., 2013. Quantitative mineralogical characterization of karst bauxite deposits in the southern Apennines. Italy. Econ. Geol. 108, 813–833.
Braun, J.J., Pagel, M., Herbillon, A., Rosin, C., 1993. Mobilization and redistribution of REEs and thorium in a syenitic lateritic profile: a mass balance study. Geochim. Cosmochim. Acta 57, 4419–4434.
Calagari, A.A., Abedini, A., 2007. Geochemical investigations on Permo-Triassic bauxite horizon at Kanisheeteh, east of Bukan, West-Azarbaidjan. Iran. J. Geochem. Explor. 94, 1–18.
Chen, C., Liu, X., Hu, Z., Zong, K., Liu, Y., 2014. In situ analysis of major and trace element composition of hydrous silicate minerals by LA-ICP-MS. Earth Sci.-J China Univ. Geosci. 39(5), 525–536 (in Chinese with English abstract).
Chen, L., Liu, Y., Hu, Z., Gao, S., Zong, K., Chen, H., 2011. Accurate determinations of fifty-four major and trace elements in carbonate by LA–ICP-MS using normalization strategy of bulk components as 100%. Chem. Geol. 284 (3–4), 283–295.
Chen, X., Zhang, Y.D., Fan, J.X., Tang, L., Sun, H.Q., 2012. Oneset of the Kwangsian Orogeny as evidenced by biofacies and lithofacies. Sci. China-Earth Sci. 55, 1592–1600.
Condie, K.C., 1993. Another look at rare-earth elements in shales. Geochim. Cosmochim. Acta 55, 2527–2531.
Deng, J., Wang, Q.F., Yang, S.J., Liu, X.F., Zhang, Q.Z., Yang, L.Q., Yang, Y.H., 2010. Genetic relationship between the Emeishan plume and the bauxite deposits in western Guangxi, China: constraints from U-Pb and Lu–Hf isotopes of the detrital zircons in bauxite ores. J. Asian Earth Sci. 37, 412–424.
Esmaeily, D., Rahimpour-Bonab, H., Esna-Ashari, A., Kananian, A., 2010. Petrography and geochemistry of the Jajarm Karst bauxite ore deposit: NE Iran: implications for source rock material and ore genesis. Turk. J. Earth Sci. 19, 267–284.
Franzini, M., Leoni, L., Saitta, M., 1972. A simple method to evaluate the matrix effects in X-ray fluorescence analysis. X-Ray Spectrom. 1, 151–154.
Gao, Z.X., Liu, B.K., 2014. Microstructure Study of Bauxite in China. Metallurgy Industry Press, Beijing, pp. 43 (in Chinese).
Gao, D., Sheng, Z., Shi, S., Chen, L., 1992. Studies on the bauxite deposit in central Guizhou, China. Guiyang, Guizhou Science & Technology Publishing House 11–20 (in Chinese).
Gu, H.N., Guo, T.F., Wen, H.J., Luo, C.G., Cui, Y., Du, S.J., 2020... Leaching efficiency of sulfuric acid on selective lithium leachability from bauxitic claystone. Miner. Eng. 145, 106076.
Gu, J., Huang, Z.L., Fan, H.P., Ye, L., Jin, Z.G., 2013. Provenance of lateritic bauxite deposits in the Wuchuan–Zheng'an–Daozhen area, northern Guizhou Province, China: LA-ICP-MS and SIMS U-Pb dating of detrital zircons. J. Asian Earth Sci. 70–71, 265–282.
Guizhou Bureau of Geology and Mineral Resources, 1987. Regional geology of Guizhou Province. Beijing, Geological Publishing House, pp. 555–557 (in Chinese).
Guizhou department of land and resource, 2012. Guizhou mineral resources bulletin.
Han, T., Fan, H., Wen, H., 2018. Dwindling vanadium in seawater during the early Cambrian, South China. Chem. Geol. 492, 20–29.
Hanilçi, N., 2013. Geological and geochemical evolution of the Bolkardaği bauxite deposits, Karaman, Turkey: Transformation from shale to bauxite. J. Geochem. Explor. 133, 118–137.
Hou, Y.L., Zhong, Y.T., Xu, Y.G., He, B., 2017. The provenance of late Permian karstic bauxite deposits in SW China, constrained by the geochemistry of interbedded clastic rocks, and U-Pb–Hf–O isotopes of detrital zircons. Lithos 278–281, 240–254.
Huang, Z.L., Jin, Z.G., Xiang, X.L., Gu, J., Wu, G.H., Chen, X.L., Su, Z.L., Zhao, Y.Y., Ye, L., Zhou, L., 2014. Metallogenic theory and prediction of bauxite deposits in the Wuchuan-Zheng'an-Daozhen area, Northern Guizhou Province. Science Press, China. Beijing, pp. 1–245 (in Chinese).
Karadağ, M.M., Küpeli, S., Arýk, F., Ayhan, A., Zedef, V., Döyen, A., 2009. Rare earth element (REE) geochemistry and genetic implications of the Mortas bauxite deposit (Seydis, ehir/Konya–southern Turkey): Chem. Erde-Geochem. 69, 143–159.
Karayigit, A.I., Bulut, Y., Karayigit, G., Querol, X., Alastuey, A., Vassilev, S., Vassilev, C., 2006. Mass balance of major and trace elements in a coal-fired power plant. Energ. Source Part A 28, 1311–1320.
Khosravi, M., Abedini, A., Alipour, S., Mongelli, G., 2017. The Darzi-Vali bauxite deposit, West-Azarbaidjan Province, Iran: critical metals distribution and parental affinities. J Afr. Earth Sci. 2017 (129), 960–972.
Konhauser, K.O., Pecoits, E., Lalonde, S.V., Papineau, D., Nisbet, E.G., Barley, M.E., Arndt, N.T., Zahnle, K., Kamber, B.S., 2009. Oceanic nickel depletion and a methanogen famine before the Great Oxidation Event. Nature 458, 750–753.
Laskou, M., Economou-Eliopoulos, M., 2013. Bio-mineralization and potential biogeochemical processes in bauxite deposits: genetic and ore quality significance. Mineral. Petrol. 107, 471–486.
Lehmann, B., Frei, R., Xu, L., Mao, J., 2016. Early Cambrian black shale-hosted Mo-Ni and V mineralization on the rifted margin of the Yangtze Platform, China: reconnaissance chromium isotope data and a refined metallogenic model. Econ. Geol. 111 (1), 89–103.
Li, Y.J., 2013. Analysis of Geochemical Characteristics and Genesis of bauxite in Guizhou.

The Master Dissertation of University of Chinese Academy of Sciences 1–82 (in Chinese).
Li, J., 2019. Geochemical and mineralization characteristics for the key bed of vanadium deposit in the base of Cambrian black rock series in Cengong, Guizhou. The Master Dissertation of Guizhou University 1–51 (in Chinese).
Li, Z.H., Din, J., Xu, J.S., Liao, C.G., Yin, F.G., Lv, T., Cheng, L., Li, J.M., 2013. Discovery of the REE minerals in the Wulong-Nanchuan bauxite deposits, Chongqing, China: Insights on conditions of formation and processes. J. Geocehm. Explor. 133, 88–102.
Ling, K.Y., Zhu, X.Q., Tang, H.S., Wang, Z.G., Yan, H.W., Han, T., Chen, W.Y., 2015. Mineralogical characteristics of the karstic bauxite deposits in the Xiuwen ore belt, Central Guizhou Province. Southwest China. Ore Geol. Rev. 65, 84–96.
Ling, K.Y., Zhu, X.Q., Tang, H.S., Li, S.X., 2017. Importance of hydrogeological conditions during formation of the karstic bauxite deposits, Central Guizhou Province, Southwest China: A case study at Lindai deposit. Ore Geol. Rev. 82, 198–216.
Ling, K.Y., Zhu, X.Q., Tang, H.S., Du, S.J., Gu, J., 2018. Geology and geochemistry of the Xiaoshanba bauxite deposit, Central Guizhou Province, SW China: Implications for the behavior of trace and rare earth elements. J Geochem. Explor. 190, 170–186.
Liu, Y.S., Hu, Z.C., Gao, S., Günther, D., Xu, J., Gao, C.G., Chen, H.H., 2008. In situ analysis of major and trace elements of anhydrous minerals by LA-ICP-MS without applying an internal standard. Chem. Geol. 257 (1–2), 34–43.
Liu, Y., Hu, Z., Zong, K., Gao, C., Gao, S., Xu, J., Chen, H., 2010. Reappraisement and refinement of zircon U-Pb isotope and trace element analyses by LA-ICP-MS. Chinese Sci. Bull. 55 (15), 1535–1546.
Liu, Y.L., Ling, M.X., Williams, I.S., Yang, X.Y., Wang, C.Y., Sun, W.D., 2018. The formation of the giant Bayan Obo REE-Nb-Fe deposit, North China, Mesoproterozoic carbonatite and overprinted Paleozoic dolomitization. Ore Geol. Rev. 92, 73–83.
Liu, X.F., Wang, Q.F., Zhang, Q.Z., Feng, Y.W., Cai, S.H., 2012. Mineralogical characteristics of the superlarge Quaternary bauxite deposits in Jingxi and Debao counties, western Guangxi. China. J. Asian Earth Sci. 52, 53–62.
Liu, X.F., Wang, Q.F., Feng, Y.W., Li, Z.M., Cai, S.H., 2013. Genesis of the Guangou karstic bauxite deposit in western Henan. China. Ore Geol. Rev. 55, 162–175.
Liu, X.F., Wang, Q.F., Zhang, Q.Z., Zhang, Y., Li, Y., 2016. Genesis of REE minerals in the karstic bauxite in western Guangxi, China, and its constraints on the deposit formation conditions. Ore Geol. Rev. 75, 100–115.
Liu, X.F., Wang, Q.F., Zhang, Q.Z., Yang, S.J., Liang, Y.Y., Zhang, Y., Li, Y., Guan, T., 2017. Genesis of the Permian karstic Pingguo bauxite deposit, western Guangxi. China. Miner. Deposita 52, 1031–1048.
Long, Y.Z., Chi, G.X., Liu, J.P., Jin, Z.G., Dai, T.G., 2017. Trace and rare earth elements constraints on the sources of the Yunfeng paleo-karstic bauxite deposit in the XiuwenQingzhen area, Guizhou. China. Ore Geol. Rev. 91, 404–418.
Long, Y., Chi, G., Liu, J., Zhang, D., Song, H., 2018. Uranium enrichment in a paleo-karstic bauxite deposit, Yunfeng, SW China: Mineralogy, geochemistry, transport—deposition mechanisms and significance for uranium exploration. J Geochem. Explor. 190, 424–435.
Lu, F.K., Huang, Z.L., Jin, Z.G., Zhou, J.X., Ding, W., Gu, Jing, 2009. A primary study on the content features and occurrence state of Gallium in bauxite from the Wuchuan-Zhengan-Daozhen area, Northern Guizhou Province. China. Acta. Miner. Sin. 29 (3), 373–379 (in Chinese with English abstract).
Int J Earth Sci (Geol Rundsch) 96 (5), 887–902. https://doi.org/10.1007/s00531-006-0142-2.
Mongelli, G., 1997. Ce-anomalies in the textural components of Upper Cretaceous karst bauxites from the Apulian Carbon ate Platform (southern Italy): Chem. Geol. 140, 69–79.
Mongelli, G., Boni, M., Buccione, R., Sinisi, R., 2014. Geochemistry of the Apulian karst bauxites (southern Italy): Chemical fractionation and parental affinities. Ore Geol. Rev. 63, 9–21.
Mongelli, G., Buccione, R., Gueguen, E., Langone, A., Sinisi, R., 2016. Geochemistry of the apulian allochthonous karst bauxite, Southern Italy: Distribution of critical elements and constraints on Late Cretaceous Peri-Tethyan palaeogeography. Ore Geol. Rev. 77, 246–259.
Mordberg, L.E., Stanley, C.J., Germann, K., 2000. Rare earth element anomalies in crandallite group minerals from the Schugorsk bauxite deposit, Timan. Russia. Eur. J. Mineral. 12, 1229–1243.
Mordberg, L.E., Stanley, C.J., Germann, A., 2001. Mineralogy and geochemistry of trace elements in bauxites: the Devonian Schugorsk deposit. Russia. Mineral. Mag. 65 (1), 81–101.
Öztürk, H., Hein, J.R., Hanilçi, N., 2002. Genesis of the Dogankuzu and Mortas Bauxite Deposits, Taurides, Turkey: Separation of Al, Fe, and Mn and implications for Passive Margin Metallogeny. Econ. Geol. 97, 1063–1077.
Pan, Z.L., Zhao, A.X., Pan, T.H., 2006. Crystallography and mineralogy. Beijing,China, Geological Publishing House, pp. 1–282.(In Chinese).
Pokrovsky, O.S., Schott, J., Dupre, B., 2006. Trace element fractionation and transport in boreal rivers and soil porewaters of permafrost-dominated basaltic terrain in Central Siberia. Geochim. Cosmochim. Acta 70, 3239–3260.
Potts, P.J., Thompson, M., Kane, J.S., Petrov, L.L., 2000. GEOPT7–an international proficiency test for analytical geochemistry laboratories. Report on Round 7, 35.
Potts, P.J., Thompson, M., Webb, P.C., Watson, J.S., 2001. GEOPT9–an international proficiency test for analytical geochemistry laboratories. Report on Round 9, 36.
Qi, L., Hu, J., Gregoire, D.C., 2000. Determination of trace elements in granites by inductively coupled plasma mass spectrometry. Talanta 51, 507–513.
Radisinović, S., Jelenković, R., Paćevski, A., Simić, V., Božović, D., Holclajtner-Antunović, I., Životić, D., 2017. Content and mode of occurrences of rare earth elements in the Zagrad karstic bauxite deposit (Nikšić area, Montenegro). Ore Geol. Rev. 80, 406–428.
Robbins, L.J., Konhauser, K.O., Warchola, T.J., Homann, M., Thoby, M., Foster, I., Mloszewska, A.M., Alessi, D.S., Lalonde, S.V., 2019. A comparison of bulk versus laser ablation trace element analyses in banded iron formations: Insights into the mechanisms leading to compositional variability. Chem. Geol. 506, 197–224.
Rong, J.Y., Chen, X., Wang, Y., Zhan, R.B., Liu, J.B., Huang, B., Tang, P., Wu, R.C., Wang, G.X., 2011. Northward expansion of Central Guizhou Oldland through the Ordovician and Silurian transition: Evidence and implications. Sci. China-Earth Sci. 41, 1407–1415 (in Chinese with English Abstract).
Takaya, Y., Yasukawa, K., Kawasaki, T., et al., 2018. The tremendous potential of deep-sea mud as a source of rare-earth elements. Sci. Rep. 8 (1), 5763.
Tang, Y.J., Liu, J.C., Jia, J.Y., 2002. Study on occurrence state of gallium in the bauxite deposit of Western Henan Province. J. Xi'an Eng. Univ. 24 (4), 1–5 (in Chinese with English abstract).
Thompson, M., Potts, P.J., Kane, J.S., Wilson, S., 1999. GEOPT5–an international proficiency test for analytical geochemistry laboratories. In: In: Report on Round, pp. 5. 23..
Wang, Q.F., Deng, J., Liu, X.F., Zhang, Q.Z., Sun, S.L., Jiang, C.Z., Zhou, F., 2010a. Discovery of the REE minerals and its geological significance in the Quyang bauxite deposit, West Guangxi. China. J. Asian Earth Sci. 39, 701–712.
Wang, Q.F., Deng, J., Liu, X.F., Zhao, R., Cai, S.H., 2016. Provenance of Late Carboniferous bauxite deposits in the North China Craton: New constraints on marginal arc construction and accretion processes. Gondwana Res. 38, 86–98.
Wang, D.H., Li, P.G., Qu, W.J., et al., 2013. Discovery and preliminary study of the high tungsten and lithium contents in the Dazhuyuan bauxite deposit, Guizhou. China. Sci. China: Earth Sci. 2013 (56), 145–152.
Wang, Q.F., Liu, X.F., Yan, C.H., Cai, S.H., Li, Z.M., Wang, Y.R., Zhao, J.M., Li, G.J., 2012. Mineralogical and geochemical studies of boron-rich bauxite ore deposits in the Songqi region, SW Henan. China. Ore Geol. Rev. 48, 258–270.
Wang, R.X., Wang, Q.F., Huang, Y.X., Yang, S.J., Liu, X.F., Zhou, Q., 2018. Combined tectonic and paleogeographic controls on the genesis of bauxite in the Early Carboniferous to Permian Central Yangtze Island. Ore Geol. Rev. 101, 468–480.
Wang, T., Zhao, X., Li, J., Lv, T., 2014. Distribution characteristics of lithium in Yinkuangyakou bauxite deposit. Chongqing. Contrib. Geol. Miner. Res. Res. 29 (4), 541–545 (in Chinese with English abstract).
Wang, Y., Zhou, L.Y., Zhao, L.J., Ji, M., Gao, H.L., 2010b. Palaeozoic uplands and unconformity in the North China Block: constraints from zircon LA-ICP-MS dating and geochemical analysis of bauxite. Terra Nova 22, 264–273.
Weng, S., Yu, W., Algeo, T.J., Du, Y., Li, P., Lei, Z., Zhao, S., 2019. Giant bauxite deposits of South China: Multistage formation linked to Late Paleozoic Ice Age (LPIA) eustatic fluctuations. Ore Geol. Rev. 104, 1–13.
Wu, S.W., Xia, Y., Xie, Z.J., He, S., Yang, H.Y., 2017. The mode of occurrence of rare earth elements in Xinhua phosphorite-type REE deposit, Zhijin, Guizhou Province. Acta Miner. Sin. S 1, 260 (in Chinese with English abstract).
Yang, X.Y., Lai, X.D., Pirajno, F., Liu, Y.L., Ling, M.X., Sun, W.D., 2017. Genesis of the Bayan Obo Fe-REE-Nb formation in Inner Mongolia, North China Craton: A perspective review. Pricambrian Res. 288, 39–71.
Yang, S.J., Wang, Q.F., Zhang, Q.Z., Chen, J.H., Huang, Y.X., 2018. Terrestrial deposition processes of Quaternary gibbsite nodules in the Youjiang Basin, southeastern margin of Tibet, and implication for the genesis of ancient karst bauxite. Sediment. Geol. 373, 292–306.
Ye, L., Pan, Z.P., Cheng, Z.T., 2008. The regularities of distribution of associated elements in Xiaoshanba bauxite deposit. Guizhou. Acta Miner. Sin. 28 (2), 105–111 (in Chinese with English abstract).
Yu, W., Wang, R., Zhang, Q., Du, Y., Chen, Y., Liang, Y., 2014b. Mineralogical and geochemical evolution of the Fusui bauxite deposit in Guangxi, South China: From the original Permian orebody to a Quarternary Salento-type deposit. J Geochem. Explor. 146, 75–88.
Yu, W., Du, Y., Zhou, Q., Jin, Z., Wang, X., Qin, Y., Cui, T., 2014a. Provenance of bauxite beds of the Lower Permian in Wuchuan–Zheng'an–Daozhen area, northern Guizhou Province: evidence from detrital zircon chronology. J Palaeogeog. 16 (1), 19–29 (in Chinese with English abstract).
Yu, W., Algeo, T.J., Du, Y.S., Zhang, Q.L., Liang, Y.P., 2016. Mixed volcanogenic–lithogenic sources for Permian bauxite deposits in southwestern Youjiang Basin, South China, and their metallogenic significance. Sdiment. Geol. 341, 276–288.
Yuste, A., Bauluz, B., Mayayo, M.J., 2017. Origin and geochemical evolution from ferrallitized clays to karst bauxite: An example from the Lower Cretaceous of NE Spain. Ore Geol. Rev. 84, 67–79.
Zamanian, H., Ahmadnejad, F., Zarasvandi, A., 2016. Mineralogical and geochemical investigations of the Mombi bauxite deposit, Zagros Mountains. Iran. Chem. Erde Geochem. 76, 13–37.
Zarasvandi, A., Carranza, E.J.M., Ellahi, S.S., 2012. Geological, geochemical, and mineralogical characteristics of the Mandan and Deh-now bauxite deposits, Zagros Fold Belt, Iran, Ore Geol. Rev. 48, 125–138.
Zhang, Z., Zhou, L., Li, Y., Wu, C., Zheng, C., 2013. The "coal-bauxite-iron" structure in the ore-bearing rock series as a prospecting indicator for southeastern Guizhou bauxite mines. Ore Geol. Rev. 53, 145–158.
Zhao, Z., Wang, D.H., Li, P.G., Lei, Z.Y., 2013. Detrital zircon U-Pb geochronology of the Dazhuyuan Formation in Northern Guizhou: Implications for bauxite mineralization. Rock Miner. Anal. 32 (1), 166–173 (in Chinese with English abstract).